Research Square

Preprints are preliminary reports that have not undergone peer review.
They should not be considered conclusive, used to inform clinical practice,
or referenced by the media as validated information.

Data informed seasonal assessment of a PV battery grid charging station for light electric vehicles with adaptive filter forecasting, state of charge and harmonic estimation

Ankita Singh
Sharda University
Manisha Rajoriya
manisha.rajoriya@sharda.ac.in
Sharda University
Sumanlata Dhar
Sharda University
Pallavi Gupta
Sharda University

Research Article

Keywords: Measured PV data, Data quality screening, Electric vehicle charging station, Battery energy storage, State-of-charge estimation, Recursive least squares, Day-ahead forecasting, Energy management, Power quality, Seasonal assessment

Posted Date: November 16th, 2026

DOI: https://doi.org/10.21203/rs.3.rs-11399297/v1

License: This work is licensed under a Creative Commons Attribution 4.0 International License.
Read Full License

Additional Declarations: No competing interests reported.

Data informed seasonal assessment of a PV battery grid charging station for light electric vehicles with adaptive filter forecasting, state of charge and harmonic estimation

Ankita Singh[1], Manisha Rajoriya[1*], Sumanlata Dhar[1], Pallavi Gupta[1]

[1*]Department of Electrical, Electronics and Communication Engineering, Sharda University, Greater Noida, Uttar Pradesh, India.

*Corresponding author(s). E-mail(s): manisha.rajoriya@sharda.ac.in;
Contributing authors: 2024105771.ankita@dr.sharda.ac.in;
suman.lata@sharda.ac.in; pallavi.gupta2@sharda.ac.in;

Abstract

Photovoltaic (PV) charging stations for light electric vehicles are commonly sized with typical-year irradiance and verified over short simulation windows, which conceals the seasonal variability that sizes storage and grid support. This study presents a dual-timescale assessment of a grid-connected charging station with a 4 kWp PV array, a 21.6 kWh lithium iron phosphate battery and four 0.8 kW charging ports. Daily energy-meter records of an operating 325 kWp car-park canopy PV plant in northern India (January–September 2026, 270 recorded days) were screened with seven IEC 61724-1-informed and statistical rules, with co-located campus meters as a reference to separate meter faults from weather. Suspect days were excluded, not altered; 257 days were retained (95.2 % coverage), and the mean specific yield changed by only 0.8 %. The retained days were capacity-scaled to 4 kWp, converted into one-minute irradiance and simulated with a 1 s average-value model; a 1 μs switching model resolved the grid-current harmonics. Over the same months, the measured mean specific yield (4.13 kWh/kWp/day) agreed with the typical-year PVsyst estimate

within 0.6 %, but monthly deviations ranged from −21 % to +27 %. Seasonal means were 3.49 (winter), 5.06 (pre-monsoon) and 3.72 kWh/kWp/day (monsoon). For an assumed demand of 11.2 e-bike sessions per valid day, PV supplied 73.7 %, the battery 22.9 % and the grid 3.3 % of the charging energy; winter and monsoon required 26–30 % battery support and accounted for nearly all grid import. Under deliberate model and sensor errors, the proposed recursive-least-squares (RLS) adaptive extended Kalman filter reduced the mean monthly state-of-charge RMSE to 0.58 %, versus 3.16 % for an extended Kalman filter. An RLS day-ahead PV forecast reduced the forecast RMSE by 10.5 % relative to persistence, yet lowered the operational energy cost by only 0.61 % under the assumed tariff. Under simulated grid-voltage distortion, a multi-resonant proportional-resonant controller achieved the lowest steady-state distortion, and RLS harmonic estimation reduced the current total harmonic distortion at 3 kW from 7.61 % to 1.74 %, with total demand distortion below 1.3 %; these are simulation-based comparisons, not an IEEE 519 compliance assessment.

Keywords: Measured PV data, Data quality screening, Electric vehicle charging station, Battery energy storage, State-of-charge estimation, Recursive least squares, Day-ahead forecasting, Energy management, Power quality, Seasonal assessment

1 Introduction

1.1 Background

The electrification of road transport moves a large share of energy demand from liquid fuels to the electricity network, and charging infrastructure has become a central part of grid planning [1, 2]. In India and other emerging markets the largest growth is in light electric vehicles: e-bikes, e-scooters, e-rickshaws and three-wheel e-autos with 48–60 V battery packs of 1–8 kWh. For these vehicles, small charging stations supplied by rooftop solar photovoltaic (PV) generation and a battery energy storage system (BESS) can deliver most of the charging energy locally, reduce the load on weak distribution feeders and lower the emission intensity of transport [8, 9, 21]. Reviews of charging technology and station architectures [1–7] identify the key building blocks of such stations: efficient DC–DC conversion, bidirectional storage interfaces, grid converters that comply with harmonic standards, and an energy management system (EMS) that coordinates PV, storage, vehicles and the grid [4, 5].

1.2 Research gap

Most PV-assisted charging station studies demonstrate their converters and control in simulation windows of a few seconds with constant or step irradiance [10, 13–19], or size the station with typical-year estimates from tools such as PVsyst [10, 21, 23]. Such evaluations confirm the operating modes of a design but do not show how much energy the station actually obtains from a real site, how often the battery reaches its limits, how much grid support is needed in winter and monsoon months, or how the grid current quality varies with the power exchanged over months of operation. In monsoon climates the solar resource changes strongly between seasons, yet station results are rarely reported by season, so the periods that decide battery size and grid support remain hidden in long-term averages. Studies that do use long horizons usually treat the battery as an ideal energy store and do not include the state-of-charge (SOC) estimation error of a real battery management system (BMS) [30–32], although the estimated SOC is what the BMS and EMS act on [44, 45]. Grid-interface studies, conversely, report harmonic distortion at a single operating point [41, 42], while the IEEE 519 total demand distortion depends on the power level and therefore on the energy profile of the station [38, 43]. Recent data-driven studies model charging demand and scheduling at the level of the regional grid [68, 69], optimise the layout of charging facilities for renewable-energy consumption [70] and forecast charging demand probabilistically [71], but they treat the station as an aggregate load and do not resolve its PV, battery and converter behaviour.

Measured generation records from operating PV plants are a valuable but imperfect input: they contain missing readings, meter faults, outages and reading-time shifts, and they are often available only as daily energy. Using them requires a transparent data-screening procedure that excludes faulty days without altering the measured values [52]. A further practical gap is that the base design of a 4 kW PV–BESS–grid station for e-bikes [10] was evaluated with a PVsyst estimate and short mode

demonstrations; its performance under measured solar conditions, with a realistic BMS and a harmonic-controlled grid interface, has not been quantified.

1.3 Contributions

This paper addresses these gaps with a data-informed, seasonal and dual-timescale assessment of a 4 kWp station: a 1 s average-value model covers months of operation, and a 1 μs switching model resolves the converter and grid-current behaviour. Compared with the reference design [10], which was evaluated with a typical-year estimate and short mode demonstrations, the present study adds measured multi-month input, seasonal results, an imperfect battery management system and a harmonic assessment over all power levels. The contributions are:

1. A transparent pipeline that screens nine months of measured daily energy of an operating 325 kWp PV plant with seven IEC 61724-1-informed and statistical rules, using co-located campus meters as a reference to separate meter faults from weather, excludes suspect days without modifying any measured value, scales the reference-plant energy by capacity to the simulated array, and converts the retained days into one-minute irradiance for a 1 s Simulink model of every valid day.
2. A seasonal assessment (winter, pre-monsoon and monsoon, following the India Meteorological Department) of the resource, the energy contribution of PV, BESS and grid, and the grid exchange, together with a matched-period comparison of the measured specific yield with the typical-year design estimate, which agrees on average but deviates by -21 % to $+27$ % from month to month.
3. A BMS combining a proposed RLS-AEKF SOC estimator (event-triggered RLS identification of the ohmic resistance, OCV-offset augmentation and plateau-aware measurement noise) with an SOC limiter, assessed against Coulomb counting, EKF and UKF under deliberate model and sensor errors.

4. A MOSFET-based grid interface with a three-level T-type inverter, in which an RLS selective harmonic estimator and a multi-resonant PR benchmark are compared at all power levels with both THD and TDD, and the results are mapped onto the monthly power profile to give estimated time-weighted distortion indices.
5. An adaptive-filter (LMS, NLMS, RLS) day-ahead PV forecast for EMS scheduling, assessed against a perfect-forecast benchmark and under several tariff scenarios, and a capability analysis for five light-EV classes.

1.4 Organisation of the paper

The remainder of the paper is organised as follows. The Related work section reviews the literature and summarises the research gap. The Methods section describes the data screening, the irradiance reconstruction, the station models with their equations, the energy management strategies, the forecasting and grid-control algorithms and the performance indices. The Results section reports the measured resource, the PV energy consistency, the energy balance, the seasonal performance, the EV service, the SOC estimation, the forecasting and energy management, the power quality, and the cost, emission and sensitivity results. The Discussion compares the results with published studies, draws implications for station design and energy management, assesses the strength of the evidence and states the limitations. The Conclusions section summarises the findings and future work. The symbol list, the full parameter list and supplementary figures are given in Additional file 1.

2 Related work

2.1 Charging infrastructure and converter technology

Rivera et al. [1] review charging infrastructure and grid integration for electromobility, covering conductive and wireless charging, power levels and grid services. Brenna et al. [2] review charging technology and propose an approach for the optimal size of

charging stations, and Leone and Longo [3] present a modular architecture for ultra-fast charging stations. Converter technology for electric mobility is reviewed by Reddy et al. [6], who highlight wide-bandgap and synchronous topologies, and by Rajendran et al. [7], who show that energy-efficient converters are central to station efficiency. Bidirectional chargers and their control for vehicle-to-grid operation are reviewed by Rana et al. [5]. Specific converter solutions include an interleaved three-port converter for an off-grid PV charging station [18], an integrated Zeta–Luo converter [19], a model-predictive three-level bidirectional converter with voltage balancing for bipolar DC microgrids [34], optimised sliding-mode control of bidirectional DC–DC converters with G2V and V2G support [35], an artificial-neural-network-controlled canonical switching converter [36] and a 5 kW wireless charger with a multi-level power-factor-correction front end [37]. These works motivate the MOSFET synchronous converters and the three-level T-type inverter used in the present station.

2.2 PV-assisted and hybrid charging stations

Tamba et al. [8] and Hossain and Cho [9] review solar-powered charging systems and their techno-economic feasibility, and conclude that measured local conditions strongly influence the share of solar energy and the economics. Singla et al. [10] designed and simulated the 4 kW PV–BESS–grid station for e-bikes that forms the reference design of this work, with five operating modes and a PVsyst yield estimate. Singh et al. [11] studied the feasibility of a grid-connected solar–wind system with a charging station, and Singh et al. [12] implemented a PV–battery and diesel-generator station. Grid-connected PV–BESS charging stations with seamless mode transitions are presented by Jain et al. [13] and Shukl and Singh [14], and an enhanced hybrid converter topology for PV–grid–EV integration by Sekhar et al. [15]. Bagherwal and Mahapatra [17] stabilise the DC bus of a solar charging station with disturbance-observer-based adaptive sliding-mode control, and Ahamed et al. [22] integrate solar and wind energy in a

DC microgrid for charging in desert environments. For maximum power point tracking (MPPT), Mazumdar et al. [20] propose a metaheuristic tracker for grid-tied stations, Tan et al. [40] use predictive control of PV-integrated chargers, and Vendoti et al. [58] report an ANFIS-based tracker for a grid-tied PV–fuel-cell–storage charging system; population-based optimisation such as particle swarm optimisation [48] is widely used for tuning such controllers. Karmakar et al. [21] analyse PV-powered charging facilities under several Indian climate conditions and show the influence of the local resource on the techno-economic outcome.

2.3 Planning, demand and energy management

Optimal sizing and location of renewable-powered stations have been addressed for hydrogen and EV charging stations [23], solar-assisted stations in urban areas [25], multiple rooftop-PV stations for reliability [26] and charging hubs around metro transit [28]. EV demand and its uncertainty are modelled with data-driven correlated generation and demand [27] and with deep-learning demand prediction [29], while distributed consensus-based power sharing between the grid and stations is proposed in [24]. Bhatti et al. [4] classify the energy management schemes of charging stations into rule-based, optimisation-based and predictive schemes, and El-Taweel et al. [16] formulate an optimisation model for stations with PV transactive energy. For fast charging, battery-enabled stations and their grid integration and supervisory control are studied by Mahfouz and Iravani [30, 31], a DC-microgrid-based fast charging station by Arya and Das [32], and grid-forming inverters that improve distribution-grid resilience by Barsali et al. [33]. From an energy-informatics perspective, Xu et al. [68] optimise vehicle charging scheduling for a regional clean-energy power supply network, Hao [69] analyses the effect of charging demand on the control of a regional grid with a high clean-energy share, Zheng and Zheng [70] use an improved particle swarm optimisation to place charging facilities so as to increase renewable-energy consumption,

and Ostermann and Haug [71] compare probabilistic forecasts of charging demand at different aggregation levels and their consequences for energy procurement.

2.4 Power quality of the grid interface

The impact of EV charging on distribution-network power quality and its mitigation are reviewed by Srivastava et al. [38], and supraharmonic emission of DC fast chargers is analysed by Rajkumar et al. [39]. Verma and Singh [41] improve the power quality of a renewable grid-interactive charging station with an adaptive SOGI-based control, and Srilakshmi et al. [42] use a hybrid-controlled unified power quality conditioner. IEEE 519 [43] specifies the limits on current distortion as total demand distortion (TDD) relative to the maximum demand current. Proportional-resonant (PR) control with harmonic compensators [60] and SOGI-based phase-locked loops [61] are the established control methods of single-phase grid converters.

2.5 Battery modelling, SOC estimation and charging

Shirguppikar et al. [44] review Li-ion battery characterisation and SOC estimation for different chemistries, and Louis and Sampathkumar [45] predict SOC with a combined Box–Jenkins and neural network model. The extended Kalman filter for BMS state and parameter estimation was established by Plett [55]. For LFP cells, whose OCV curve is flat over most of the SOC range, Lu et al. [57] propose an adaptive EKF whose gain is tuned by particle swarm optimisation on the OCV plateau and report a maximum error below 2 % on laboratory test profiles. Multi-stage constant-current constant-voltage (CC-CV) charging [46] and charging strategies that consider temperature rise [47] define the charging profile of the vehicle batteries. MATLAB/Simulink reference models for DC fast chargers, battery modules and PV systems with MPPT [49–51] support the implementation of such stations.

2.6 Summary of related work

Table 1 summarises representative studies. The literature provides mature converter, MPPT, PQ and SOC-estimation techniques, but they are usually evaluated in isolation, over short time windows, and with idealised or typical-year solar input. A station-level study that combines measured multi-month PV data reported by season, a realistic BMS with SOC estimation error, a harmonic-controlled grid interface assessed over the actual power profile, and a forecast-based EMS is not available for light-EV charging. The present work addresses this gap.

3 Methods

3.1 Research workflow

The study evaluates a 4 kWp solar PV, BESS and grid-connected EV charging station whose ratings follow the reference design of Singla et al. [10], and drives it with nine months of measured daily generation data from an operating 325 kWp car-park canopy PV plant on a university campus in the National Capital Region of India. The complete workflow is shown in Fig. 1. Measured daily plant energy is screened with IEC 61724-1-informed and statistical data-quality rules [52, 63]; the retained days are converted into one-minute plane-of-array irradiance and ambient temperature profiles; a stochastic EV demand model and a digital-signal-processing (DSP) day-ahead PV forecaster supply the remaining inputs; and the station is simulated in two complementary MATLAB/Simulink R2026b models [49–51]. The assessment is dual-timescale. An average-value model with a fixed 1 s step simulates every valid day of January–September 2026 and yields the energy, economic, battery management and EV service results. A Simscape Electrical switching model with a 1 μs step and 20 kHz pulse-width modulation (PWM) resolves the MOSFET converters, the isolated

Table 1 Summary of related studies and the gap addressed in this work.

Ref.	Focus	Method or contribution	Aspect not covered, addressed here
[10]	4 kW PV–BESS–grid station for e-bikes	Five operating modes, MATLAB simulation, PVsyst yield estimate	Measured solar input, SOC estimation, PQ, multi-month operation
[13, 14]	Grid-connected PV–BESS charging stations	Seamless grid connection, converter control	Long-horizon energy and BMS assessment
[15, 19, 34]	Converter topologies	Hybrid converter, Zeta–Luo converter, three-level converter	Station-level energy and PQ over months
[20, 40, 58]	MPPT and control	Metaheuristic, predictive and ANFIS-based tracking	Tracking over measured daily resource
[21]	Indian climate techno-economics	PV-powered charging facility analysis	Device-level model, BMS and PQ
[30–32]	Battery-enabled fast charging	Grid integration and supervisory control	Light-EV solar station, SOC error
[41, 42]	Power quality of charging stations	Adaptive SOGI control, UPQC	TDD over all power levels and months
[44, 55, 57]	SOC estimation	Reviews, EKF, adaptive EKF for LFP	Integration with BMS limiter and EMS in a station
[4, 16]	Energy management	Classification, optimisation model	Forecast-based scheduling with a perfect-forecast bound
[68–71]	Data-driven charging scheduling, demand and layout	Regional scheduling, grid-control impact, PSO layout optimisation, probabilistic demand forecasting	Station-level PV–BESS operation with measured seasonal data

dual active bridge (DAB) and the single-phase three-level T-type inverter, and provides the grid-current harmonic behaviour, which is mapped onto the monthly power flow. The results are assessed with recognised indices and reference values, without claiming formal compliance: NMBE and CV(RMSE) as defined in ASHRAE Guideline 14 [53], IEC 61724-1 [52], IEEE 519 [43] and EN 50530 [62], and they are reported for the whole period and by season.

Table 2 classifies every input and result of the study by its origin, so that measured, derived, simulated and scenario quantities are kept apart in the interpretation of the results.

Table 2 Data provenance and evidence type of the inputs and results.

Quantity	Origin	Evidence type	Use in the study and limitation
Reference PV energy (P1, 325 kWp car-park canopy)	plant energy meter, daily readings	measured	screened; no value altered; January–September 2026
Co-located campus meters (P2–P16)	daily meter readings	measured	screening reference only (campus median); not a model input
PV energy of the 4 kWp array	P1 record	derived	capacity-scaled; not a direct measurement of a 4 kWp array
One-minute irradiance and temperature	clear-sky model scaled to the measured daily yield	derived	not an independent validation input
Day-ahead PV forecast	adaptive filters applied to the measured daily yield	derived	causal (past days only); evaluated on the 257 valid days
EV arrivals and energy demand	stochastic demand model	assumed scenario	no measured arrival, dwell-time or vehicle-mix data
Station energy flows, true BESS SOC	1 s average-value model	simulated	depends on the assumed EV demand and EMS settings
SOC estimator outputs	CC, EKF, UKF, RLS-AEKF	simulated	battery tests or hardware-in-the-loop still required
Grid-current harmonics	1 μs switching model, 8 power levels $\times$ 4 cases	simulated	steady state; assumed maximum demand current and grid-voltage distortion
Tariff and export credit	time-of-day tariff	assumed scenario	not a regulatory tariff study
CO_2 emission factor	national grid database [66], $\pm$10 %	published value with assumed bounds	sensitivity bounds, not confidence limits

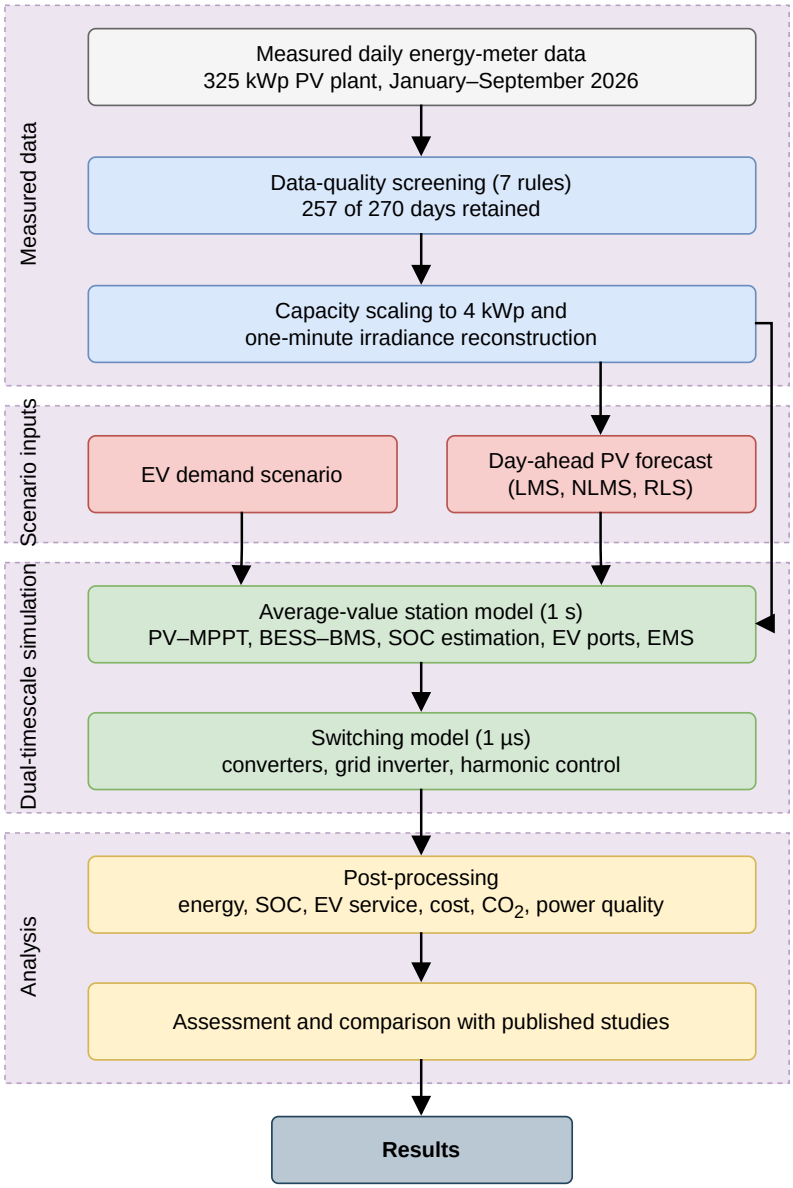


Fig. 1 Research methodology flowchart. The details of each step are given in the Methods section.

3.2 Station architecture and Simulink implementation

The station architecture is shown in Fig. 2. A 4 kWp array of sixteen SunPower SPR-E20-250 modules (four in series, four strings in parallel) feeds a 58 V DC bus through a synchronous buck converter in which the freewheeling diode of the reference design [10]

is replaced by a MOSFET, reducing conduction losses [6, 7]. A 48 V, 450 Ah LFP BESS is connected through a bidirectional synchronous buck–boost converter that regulates the bus. Four charging ports, each a synchronous buck converter with CC-CV control, serve 48 V-class two- and three-wheelers [46]. The grid interface consists of an isolated DAB with a 1:14 high-frequency transformer, an 800 V split DC link and a single-phase three-level T-type inverter with an LCL filter [34], connected to a 230 V, 50 Hz grid. The control layer contains the perturb-and-observe (P&O) MPPT [20, 40], the BMS with the proposed SOC estimator and SOC limiter, the EMS, the DSP PV forecaster, and the grid controller with a second-order generalised integrator phase-locked loop (SOGI-PLL) [61], PR current control [60] and recursive-least-squares (RLS) harmonic feed-forward.

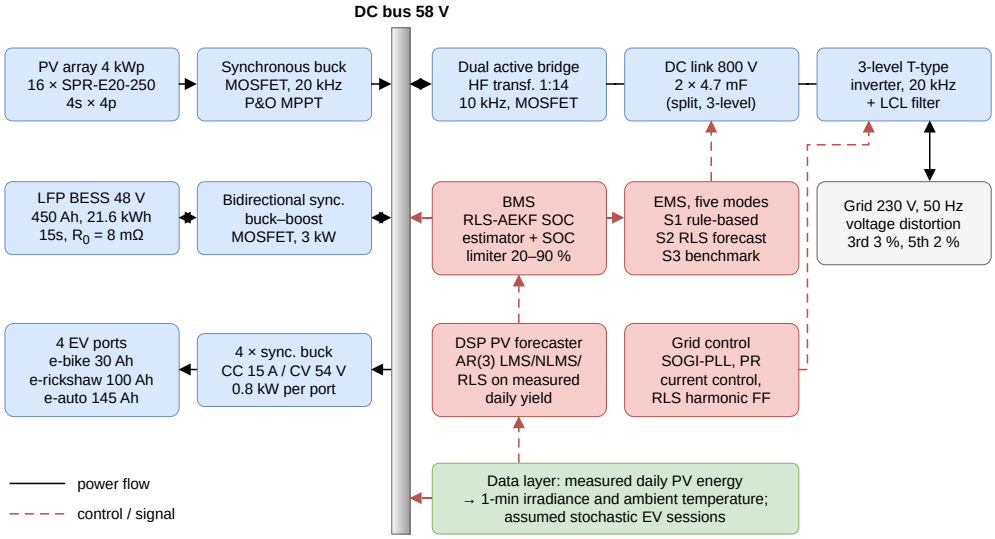


Fig. 2 Block diagram of the hybrid EV charging station showing the power stage and the control and data layers.

The average-value Simulink model (Additional file 1: Fig. S1) is built from MATLAB Function blocks executed at 1 s: PV array with MPPT, four-port EV charger, EMS, BMS SOC limiter, BESS plant, BMS SOC estimators, and the grid interface with energy meter. Irradiance and ambient temperature enter through From Workspace

blocks; EV sessions, the day-ahead forecast, the EMS strategy and the battery capacity enter as constants, so that every scenario uses the same compiled model. Signals are logged every 60 s. The switching model (Additional file 1: Fig. S2) contains the same power stage at device level and the digital controllers sampled at 20 kHz.

3.3 Measured solar data and data-quality screening

The input data are the daily energy-meter readings of an operating 325 kWp car-park canopy PV plant (the reference plant, P1) on a university campus in the National Capital Region of India, for 1 January to 27 September 2026 (270 days), the last date available in the meter register at the time of analysis. The meter registers already include the current-transformer multipliers. The daily readings of the 15 other PV installations on the same campus (P2–P16) are used only as a screening reference through the campus median of Eq. (2); they are not inputs of the station model. Their capacity history and plant-day accounting are given in Additional file 1: Table S5. The daily specific yield of plant p on day d is

$$Y_{p,d} = \frac{E_{p,d}}{P_{STC,p}}, \qquad E_{4,d} = Y_{1,d}\, P_{arr} \tag{1}$$

where $E_{p,d}$ is the daily energy (kWh), $P_{STC,p}$ the rated capacity (kWp), and $E_{4,d}$ the energy of plant P1 scaled by capacity to the simulated array $P_{arr} = 4$ kWp. The scaling assumes that the 4 kWp array has the specific yield of P1, i.e. the same orientation, shading, soiling and availability; capacity scaling does not reproduce plant-specific tilt, shading, inverter clipping or array mismatch of a smaller array. The 325 kWp car-park canopy plant P1, which has the most complete record and the highest mean yield, is the reference plant that drives the station model. Following IEC 61724-1 [52], each plant-day is screened by seven rules. A flagged day is excluded from the simulation; no measured value is modified, filled or interpolated:

1. missing or incomplete reading;

2. physical range, $Y_{p,d} < 0$ or $Y_{p,d} > 0.95\, H_{cs,d}$, where $H_{cs,d}$ is the clear-sky plane-of-array insolation (kWh/m^2) from the irradiance reconstruction described below;
3. campus-wide outage, when more than 70 % of the plants read less than 0.05 kWh/kWp on the same day;
4. plant outage, $Y_{p,d} < 0.05\, \widetilde{Y}_d$ while $\widetilde{Y}_d > 0.3$ kWh/kWp;
5. stuck register, identical non-zero meter energy on consecutive days;
6. meter-reading time shift, a low/high pair on consecutive days whose combined performance index is normal;
7. Hampel outlier [63] of the performance index on days with $\widetilde{Y}_d \geq 1.5$ kWh/kWp.

The campus median yield and the performance index are

$$\widetilde{Y}_d = median_p\left(Y_{p,d}\right), \qquad PI_{p,d} = \frac{Y_{p,d}}{\widetilde{Y}_d} \tag{2}$$

and the Hampel rule over a 21-day moving window is

$$\left|PI_{p,d} - med_{21}\left(PI_p\right)\right| > \max\left(3 \times 1.4826\, MAD_{21},\ 0.15\, med_{21}\right) \tag{3}$$

Because the performance index removes the common weather signal, rules 6 and 7 isolate meter and plant faults while cloudy and rainy days remain in the data set. The share of retained days is reported as data coverage; it is not an IEC 61724-1 compliance determination. The data are historical daily meter readings, not real-time measurements. All nine months are reported; no month or day is selected on the basis of its result. The months are grouped into the seasons of the India Meteorological Department [67]: winter (January–February), pre-monsoon (March–May) and south-west monsoon (June–September); the post-monsoon season (October–December) is outside the record. For the time-series figures, one representative month per season is used (January, May and August), and representative days are selected objectively by ranking the valid days of that month by measured yield (highest, median and lowest).

3.4 Irradiance and temperature reconstruction

The measured data are daily energies, whereas the station model requires a time series. One-minute plane-of-array irradiance is therefore reconstructed for each valid day from a clear-sky model and the measured daily yield. For day number n and Indian Standard Time t_{IST} at latitude $\varphi = 28.47^\circ$ N and longitude $\lambda = 77.48^\circ$ E [59]:

$$\begin{aligned} \delta &= 23.45^\circ \sin\left(\frac{360^\circ\,(284+n)}{365}\right), \\ EoT &= 9.87\sin 2B - 7.53\cos B - 1.5\sin B, \quad B = \frac{360^\circ\,(n-81)}{364} \end{aligned} \tag{4}$$

$$t_s = t_{IST} + \frac{4\,(\lambda - 82.5^\circ) + EoT}{60}, \qquad \omega = 15^\circ\,(t_s - 12) \tag{5}$$

$$\begin{aligned} \cos\theta_z &= \sin\varphi\sin\delta + \cos\varphi\cos\delta\cos\omega, \\ \cos\theta_i &= \sin(\varphi-\beta)\sin\delta + \cos(\varphi-\beta)\cos\delta\cos\omega \end{aligned} \tag{6}$$

where $\beta = 25^\circ$ is the south-facing tilt. The clear-sky beam irradiance follows the Meinel model [64] with a diffuse fraction of 10 %, and the plane-of-array irradiance uses the isotropic sky model with ground albedo $\rho = 0.2$:

$$DNI = 1367 \times 0.7^{\,AM^{0.678}}, \qquad AM = \frac{1}{\cos\theta_z}, \qquad DHI = 0.1\,DNI \tag{7}$$

$$G_{cs} = DNI\,\max(\cos\theta_i, 0) + DHI\,\frac{1+\cos\beta}{2} + \rho\,GHI\,\frac{1-\cos\beta}{2} \tag{8}$$

The daily clearness index scales the clear-sky profile so that the reconstructed insolation equals the measured energy divided by the reference performance ratio $PR_{ref} = 0.80$ (IEC 61724-1, $PR = Y_f/Y_r$ [52]):

$$k_d = \frac{Y_d/PR_{ref}}{H_{cs,d}}, \qquad G(t) = k_d\,G_{cs}(t) \tag{9}$$

On days with $k_d < 0.7$, first-order low-pass noise with amplitude $0.8\,(0.7 - k_d) + 0.15$ represents cloud variability, and the profile is rescaled to preserve the daily energy. The irradiance is limited to 1150 W/m^2. Ambient temperature follows a cosine diurnal profile between the monthly minimum and maximum, and the cell temperature is

$$T_c = T_a + \frac{NOCT - 20}{800}\, G \tag{10}$$

with NOCT = 45 °C. Because the intra-day profile is reconstructed, three alternative intra-day shapes with the same daily energy (smooth, high variability, morning-skewed) and PR_{ref} of 0.75 and 0.85 are used in the robustness study (see the sensitivity results).

3.5 PV array and MPPT

The array uses the single-diode model of the Simscape Solar Cell block [51] with $N_s = 288$ series cells and $N_p = 4$ strings:

$$I = N_p \left[I_{ph} - I_s \left(\exp\left(\frac{V}{N_s\, n\, V_t} \right) - 1 \right) \right], \qquad V_t = \frac{kT}{q} \tag{11}$$

$$\begin{aligned} I_{ph} &= I_{sc}\, \frac{G}{1000}\, \left[1 + \alpha_I\, (T_c - T_{ref}) \right], \\ I_s &= I_{s,ref} \left(\frac{T}{T_{ref}} \right)^{XTI/n} \exp\left[\left(\frac{T}{T_{ref}} - 1 \right) \frac{E_g}{n\, V_t} \right] \end{aligned} \tag{12}$$

with $n = 1.5$, $XTI = 3$ and $E_g = 1.11$ eV. A DC derate of 0.90 accounts for soiling, mismatch, wiring and light-induced degradation [54]. The P&O tracker updates the voltage reference every second,

$$V_{ref}(k{+}1) = V_{ref}(k) + \Delta V\; sgn\left[(P(k) - P(k-1))\, (V(k) - V(k-1)) \right], \qquad \Delta V = 1\, V \tag{13}$$

starts each morning at $0.8\,V_{oc}$, and enters a power-limiting mode when the EMS issues a curtailment command. The tracking efficiency (EN 50530 [62]) is

$$\eta_{MPPT} = \frac{\int P_{pv}\,dt}{\int P_{mpp}\,dt} \tag{14}$$

where P_{mpp} is obtained by golden-section search on Eq. (11). Every converter is represented by the loss model

$$P_{loss} = P_0 + k\,P^2 \tag{15}$$

whose coefficients were fitted to the switching model (PV buck 97 %, BESS converter 96.5 %, EV charger 96 % and grid interface 94 % at rated power; Additional file 1: Table S2).

3.6 Battery energy storage and BMS SOC limiter

The 48 V LFP pack (15 cells in series, 450 Ah, 21.6 kWh) is represented by a first-order Thevenin model with an LFP open-circuit-voltage (OCV) curve [44, 50]:

$$v_b = N_s\,OCV(SOC) + v_{RC} + R_0\,i_b \tag{16}$$

$$v_{RC}(k+1) = a\,v_{RC}(k) + R_1(1-a)i_b(k), \qquad a = e^{-\Delta t/\tau} \tag{17}$$

$$SOC(k+1) = SOC(k) + \frac{i_b(k)\,\Delta t}{3600\,Q} \tag{18}$$

with $R_0 = 8$ mΩ, $R_1 = 4$ mΩ, $\tau = 60$ s and $\Delta t = 1$ s. Because the BESS converter regulates the DC bus, its bus-side power closes the power balance:

$$P_b = P_{pv} - P_{ev} - P_g \tag{19}$$

The proposed BMS SOC limiter keeps the battery inside the 20–90 % operating window of the reference design [10] by de-rating the allowed power linearly over a 2 % band on the estimated SOC:

$$\begin{aligned} P_{ch,lim} &= P_{ch,\max}\, sat_{[0,1]}\left(\frac{SOC_{\max} - \widehat{SOC}}{0.02}\right), \\ P_{dis,lim} &= P_{dis,\max}\, sat_{[0,1]}\left(\frac{\widehat{SOC} - SOC_{\min}}{0.02}\right) \end{aligned} \tag{20}$$

with $P_{ch,\max} = P_{dis,\max} = 3$ kW (0.15C). An independent cell-voltage trip (3.45 V/cell for charge, 3.10 V/cell for discharge) provides back-up protection.

3.7 SOC estimation

Four estimators run in parallel on noisy measurements $v_m = v_b + n_v$ and $i_m = i_b + b_i + n_i$ ($\sigma_v = 0.05$ V, $\sigma_i = 0.5$ A, current-sensor bias $b_i = 0.1$ A). All estimators use a model that deliberately differs from the plant (capacity -5 %, R_0 $+30$ %, OCV offset $+5$ mV/cell, initial SOC 0.45 against the true 0.60), which reproduces typical BMS uncertainty [44, 55]. The true SOC is available from the plant model, so the estimation error can be computed exactly; the assessment is therefore a simulation study of robustness to these errors.

Coulomb counting (CC):

$$\widehat{SOC}(k+1) = \widehat{SOC}(k) + \frac{i_m(k)\,\Delta t}{3600\,\widehat{Q}} \tag{21}$$

Extended Kalman filter (EKF) [55] with state $\mathbf{x} = [SOC,\ v_{RC}]^T$:

$$\mathbf{x}^- = \mathbf{A}\mathbf{x} + \mathbf{B}i_m, \qquad \mathbf{P}^- = \mathbf{A}\mathbf{P}\mathbf{A}^T + \mathbf{Q}, \qquad \mathbf{A} = \begin{bmatrix} 1 & 0 \\ 0 & a \end{bmatrix}, \quad \mathbf{B} = \begin{bmatrix} \Delta t / \left(3600\widehat{Q}\right) \\ R_1(1-a) \end{bmatrix} \tag{22}$$

$$\begin{aligned}\mathbf{K} &= \mathbf{P}^{-}\mathbf{H}^{T}\left(\mathbf{H}\mathbf{P}^{-}\mathbf{H}^{T}+R\right)^{-1},\\ \mathbf{x} &= \mathbf{x}^{-}+\mathbf{K}\left(v_m-h\left(\mathbf{x}^{-}\right)\right),\\ \mathbf{P} &= \left(\mathbf{I}-\mathbf{K}\mathbf{H}\right)\mathbf{P}^{-}\end{aligned} \tag{23}$$

where $h(\mathbf{x}) = N_s\,OCV(SOC) + v_{RC} + \widehat{R}_0 i_m$ and $\mathbf{H} = \partial h/\partial \mathbf{x}$.

Unscented Kalman filter (UKF) with $2n+1$ sigma points, $\chi_0 = \mathbf{x}$, $\chi_i = \mathbf{x} \pm \left(\sqrt{(n+\lambda)\mathbf{P}}\right)_i$, $\lambda = \alpha^2(n+\kappa) - n$, $\alpha = 0.5$, $\beta_u = 2$, $\kappa = 1$.

Proposed RLS-AEKF. The proposed estimator combines online identification of the ohmic resistance with an augmented EKF. An event-triggered RLS estimator with forgetting factor $\lambda_R = 0.9999$ updates $\widehat{R}_0$ only on current steps $|\Delta i_m| > 8$ A, where the voltage step is dominated by the ohmic drop:

$$\begin{aligned} g(k) &= \frac{P_R\,\Delta i_m(k)}{\lambda_R + \Delta i_m(k)\,P_R\,\Delta i_m(k)},\\ \widehat{R}_0(k) &= \widehat{R}_0(k-1) + g(k)\left[\Delta v_m(k) - \widehat{R}_0(k-1)\,\Delta i_m(k)\right]\end{aligned} \tag{24}$$

$$P_R(k) = \frac{P_R(k-1) - g(k)\,\Delta i_m(k)\,P_R(k-1)}{\lambda_R} \tag{25}$$

The state is augmented with an OCV offset Δ_{ocv} that absorbs the OCV-curve error, $\mathbf{x}_a = [SOC,\ v_{RC},\ \Delta_{ocv}]^T$, with

$$h_a(\mathbf{x}_a) = N_s\,OCV(SOC) + v_{RC} + \widehat{R}_0\,i_m + \Delta_{ocv} \tag{26}$$

Because the LFP OCV curve is nearly flat between 30 % and 80 % SOC, the voltage carries little SOC information on this plateau. A plateau-aware measurement noise therefore weights the voltage innovation by the local OCV slope $s_{cell} = dOCV/dSOC$ per cell:

$$R_{eff} = R + 10^{-3}\left(\frac{0.06}{\max\left(s_{cell}, 0.02\right)}\right)^2 \tag{27}$$

The estimate of the proposed RLS-AEKF drives the BMS limiter and the EMS. Accuracy is reported as RMSE and maximum absolute error after a 72 h convergence window from the deliberately wrong initial SOC, together with the convergence time.

3.8 EV charging ports and demand model

Each port is a CC-CV charger rated at 15 A / 54 V (0.8 kW). The EV battery follows the Simscape battery characteristic [50]

$$OCV_{ev}(x) = \frac{V_{full}\, x}{1 - \beta_{ev}(1-x)}, \qquad \beta_{ev} = \frac{1 - V_{full} x_1 / V_1}{1 - x_1} \tag{28}$$

and the charging current is

$$I_{ch} = \min\left(I_{cc},\ \frac{V_{cv} - OCV_{ev}(x)}{R_{ev}}\right) \tag{29}$$

A session ends when $I_{ch} < I_{\min} = 1.5$ A or the target SOC is reached; a vehicle that has not finished by its departure time leaves partially charged. Vehicles are queued first-come-first-served on the four ports. No measured EV charging records are available for the site; the EV demand is therefore an assumed scenario that follows the 10–12 EVs/day of the reference design [10]: 12 e-bikes (48 V, 30 Ah) per weekday and 6 on Sundays, 60 % arriving 08:00–11:00 and 40 % 12:00–17:00, arrival SOC uniformly 20–40 %, target 95 % and a 4 h maximum stay. Higher demand levels and a mixed fleet are examined in the sensitivity study. The vehicle classes of the capability study are given in Table 3. The e-auto parameters correspond to a 48 V, 7.4 kWh three-wheeler [65].

3.9 Energy management system

The EMS reproduces the five operating modes of the reference design [10] (PV→BESS, PV→EV, grid→EV, BESS→EV, PV→grid) and adds grid→BESS pre-charging. On the actual PV power, with net power $P_{net} = P_{pv} - P_{ev}$:

Table 3 Vehicle classes considered in the capability study.

Vehicle	Battery (kWh)	Charged fraction	Energy per charge (kWh)	Charging time, 0.8 kW port (h)
E-bike, 48 V 30 Ah	1.44	0.70	1.05	1.3
E-scooter, ˜60 V 40 Ah	2.50	0.70	1.82	2.3
E-rickshaw, 48 V 100 Ah	4.80	0.75	3.75	4.7
E-auto, 48 V 7.4 kWh [65]	7.40	0.55	4.24	5.3
Small e-car, ˜22 kWh (3.3 kW AC)	21.6	0.50	11.25	3.4

$$P_b = \begin{cases} \min\left(P_{net},\, P_{ch,lim}\right), & P_{net} \geq 0 \\ -\min\left(\left|P_{net}\right|,\, P_{dis,lim}\right), & P_{net} < 0 \end{cases}$$
$$P_g = \begin{cases} \min\left(P_{net} - P_b,\, P_{\mathrm{exp,max}}\right), & P_{net} \geq 0 \\ -\min\left(\left|P_{net}\right| - \left|P_b\right|,\, P_{imp,\mathrm{max}}\right), & P_{net} < 0 \end{cases} \tag{30}$$

Surplus beyond the BESS and export limits is curtailed through the PV power-limiting mode. Three strategies are compared:

- **S1, rule-based:** Eq. (30) only.
- **S2, RLS forecast:** during 00:00–05:00 the BESS is pre-charged from the grid at the off-peak tariff if the forecast energy deficit of the coming day is positive:

$$D_d = E_{dem,d} - \eta_{sys}\,\widehat{E}_{pv,d} - m, \qquad SOC_t = \min\left(SOC_{\max} - 0.02,\; SOC_{\min} + \frac{D_d}{E_{nom}}\right) \tag{31}$$

where $\widehat{E}_{pv,d}$ is the RLS day-ahead forecast, $\eta_{sys} = 0.9$ and the forecast-uncertainty margin is $m = 2.5$ kWh.

- **S3, perfect-forecast benchmark:** as S2 with the measured energy of the coming day and $m = 0$. S3 gives the upper bound of the saving attainable by forecast-based scheduling.

The net energy cost over a horizon uses an assumed time-of-day (ToD) tariff, Rs 7.0/kWh base, $\times 1.20$ during 18:00–22:00 and $\times 0.85$ during 22:00–06:00, and an export credit of Rs 3.0/kWh:

$$C = \sum_t c(t)\, P_{imp}(t)\, \Delta t - c_{\text{exp}} \sum_t P_{\text{exp}}(t)\, \Delta t \tag{32}$$

A grid-only station supplying the same EV energy through the same grid interface is the economic reference.

3.10 DSP day-ahead PV forecasting

The day-ahead specific yield is predicted with adaptive linear predictors of order three on the mean-removed series of valid reference-plant days [56]:

$$\widehat{y}(d) = \bar{y} + \mathbf{w}^T(d)\, \mathbf{x}(d), \qquad \mathbf{x}(d) = [y(d-1) - \bar{y},\ y(d-2) - \bar{y},\ y(d-3) - \bar{y},\ 1]^T \tag{33}$$

With the prediction error $e(d) = y(d) - \widehat{y}(d)$, the weights are updated after each day by

$$\text{LMS: } \mathbf{w} \leftarrow \mathbf{w} + \mu\, e\, \mathbf{x}; \qquad \text{NLMS: } \mathbf{w} \leftarrow \mathbf{w} + \frac{\mu\, e\, \mathbf{x}}{\varepsilon + \mathbf{x}^T\mathbf{x}} \tag{34}$$

$$\text{RLS: } \mathbf{g} = \frac{\mathbf{P}\mathbf{x}}{\lambda + \mathbf{x}^T\mathbf{P}\mathbf{x}}, \qquad \mathbf{w} \leftarrow \mathbf{w} + \mathbf{g}\, e, \qquad \mathbf{P} \leftarrow \frac{\mathbf{P} - \mathbf{g}\mathbf{x}^T\mathbf{P}}{\lambda} \tag{35}$$

with $\mu_{LMS} = 0.005$, $\mu_{NLMS} = 0.3$ and $\lambda = 0.98$. Persistence and a 7-day moving average are the reference predictors, and the predictor with the lowest RMSE (RLS)

drives strategy S2. All predictors are causal: the forecast for day d uses only valid days before d, and the weights are updated only after the measured yield of day d is known, so no future information enters the forecast or the EMS.

3.11 Grid interface and power-quality control

The DAB transfers power between the 58 V bus and the 800 V DC link by single-phase-shift control:

$$P_{DAB} = \frac{V_1\,(V_2/N)}{2\,f_s\,L_k}\,d\,(1-|d|)\,, \qquad d = \frac{\varphi}{\pi} \tag{36}$$

with $N = 14$, $f_s = 10$ kHz and $L_k = 8$ μH. The three-level T-type inverter injects the grid current through an LCL filter whose resonance frequency is

$$f_{res} = \frac{1}{2\pi}\sqrt{\frac{L_1 + L_2}{L_1\,L_2\,C_f}} = 2.52\ kHz \tag{37}$$

for $L_1 = 2$ mH, $L_2 = 0.5$ mH and $C_f = 10$ μF, with passive damping $R_d = 2.1$ Ω. The current reference is synchronised by a SOGI-PLL [61] and tracked by a PR controller [60]:

$$G_{PR}(s) = K_p + \frac{2K_r\,\omega_c\,s}{s^2 + 2\omega_c\,s + \omega_0^2} \tag{38}$$

with $K_p = 8$, $K_r = 400$ and $\omega_c = 5$ rad/s. To test harmonic rejection, the grid voltage is assumed to contain 3 % third and 2 % fifth harmonics. Two compensation methods are compared. The **proposed RLS harmonic estimator** identifies the grid-voltage harmonics $h \in \{1, 3, 5, 7, 9, 11\}$ online from the regressor $\phi(\theta) = [\sin h\theta,\ \cos h\theta]^T$, using the update of Eq. (35) with $\lambda = 0.999$, covariance symmetrisation and anti-windup reset, and feeds the estimated harmonic voltage forward with a 1.5-sample delay compensation:

$$v_{ff} = \sum_{h \neq 1} \widehat{\mathbf{w}}_h^T \, \phi_h \left(\theta + 1.5\,\omega T_s\right) \tag{39}$$

The **benchmark** is the conventional multi-resonant harmonic compensator [41, 60]:

$$G_{PR+HC}(s) = G_{PR}(s) + \sum_{h=3,5,7} \frac{2K_h\,\omega_c\,s}{s^2 + 2\omega_c\,s + (h\,\omega_0)^2}, \qquad K_{3,5,7} = 150,\ 100,\ 60 \tag{40}$$

Each case is simulated at eight constant grid powers from −3 kW (import) to +3 kW (export) for 0.5 s, and the indices are evaluated over the last five cycles by FFT [43]:

$$THD_i = \frac{\sqrt{\sum_{h\geq 2} I_h^2}}{I_1}, \qquad TDD = \frac{\sqrt{\sum_{h\geq 2} I_h^2}}{I_L}, \qquad PF = \frac{P}{V_{rms}\,I_{rms}} \tag{41}$$

where $I_L = 4000/230 = 17.4$ A is the maximum demand current. The TDD and THD curves versus grid power are interpolated onto the one-minute grid power of the monthly simulation to obtain estimated time-weighted monthly indices:

$$\overline{TDD} = \frac{\sum_{t\in\mathcal{A}} TDD\left(P_g(t)\right)}{|\mathcal{A}|}, \qquad \mathcal{A} = \{t : |P_g(t)| \geq 50\ W\} \tag{42}$$

3.12 Simulation parameters

All parameters of both models are listed in Additional file 1: Table S2 together with their sources; the main values are given in the preceding subsections. The average-value model is simulated for every valid day of each month (31, 28, 30, 28, 31, 27, 29, 30 and 23 days for January–September), for strategies S1–S3, giving 27 monthly simulations. Ten additional January simulations form the sensitivity and robustness

study. The switching model is evaluated at 32 operating points (8 power levels × 4 grid and control cases).

3.13 Performance indices

The agreement between the model PV energy and the measured energy is expressed with the indices defined in ASHRAE Guideline 14 [53]:

$$\begin{aligned} NMBE &= \frac{\sum_{i=1}^{n} (\widehat{y}_i - y_i)}{n\,\bar{y}} \times 100\,\%, \\ CV(RMSE) &= \frac{\sqrt{\sum_{i=1}^{n} (\widehat{y}_i - y_i)^2 / (n-1)}}{\bar{y}} \times 100\,\% \end{aligned} \tag{43}$$

Because the reconstructed irradiance is derived from the measured daily yield, these indices are an energy-consistency check of the reconstruction and the PV model chain, not an independent validation of the irradiance. The DC-bus energy closure and the station efficiency are

$$\varepsilon = \frac{|E_{in} - E_{out}|}{E_{in}}, \qquad \eta_{st} = \frac{E_{ev} + E_{\mathrm{exp}} + \Delta E_{BESS}}{E_{pv,dc} + E_{imp}} \tag{44}$$

The local (PV and BESS) share of EV energy and the avoided emission, with the Indian grid weighted-average emission factor $EF = 0.727$ $\mathrm{kgCO_2/kWh}$ [66], are

$$s_{loc} = \frac{E_{pv\to ev} + E_{b\to ev}}{E_{ev,bus}}, \qquad m_{CO_2} = E_{ev}\, s_{loc}\, EF \tag{45}$$

Seasonal means are given with an independence-based 95 % half-width, and the typical-year estimate of the reference design is converted, month by month, into a daily specific yield and weighted by the valid days of each month, so that it covers the same months as the measured record:

$$\bar{Y}_s = \frac{1}{n_s}\sum_{d\in s} Y_{1,d}, \qquad CI_{95} = \frac{1.96\,\sigma_s}{\sqrt{n_s}}, \qquad \bar{Y}_{PVsyst} = \frac{\sum_m n_m\, H_{inc,m}\, PR_m/N_m}{\sum_m n_m} \tag{46}$$

In Eq. (46), $H_{inc,m}$ and PR_m are the monthly plane-of-array insolation and performance ratio of the PVsyst report of [10], N_m the number of days and n_m the number of valid days of month m. The confidence half-width of Eq. (46) assumes independent days. Because consecutive production days are correlated (lag-1 autocorrelation 0.38–0.51 within the seasons), this half-width is reported only as a descriptive value, and the seasonal comparison uses a moving-block bootstrap [72] with 7-day blocks, 10 000 resamples and percentile intervals. For the grid current, the maximum demand current I_L is not measured, and the short-circuit ratio I_{SC}/I_L at the point of common coupling is unknown. The results are therefore compared with comparison lines taken from the most stringent IEEE 519-2022 limits for low-voltage systems [43], which apply to $I_{SC}/I_L < 20$: TDD 5 % and individual odd harmonics below the 11th 4 %, with an assumed $I_L = 17.4$ A from Eq. (41). A formal assessment requires the measured I_{SC}/I_L and the duration-based statistics of the standard, so no compliance is claimed. Further criteria are the EN 50530 tracking efficiency [62], full charging of at least 99 % of EV sessions and the 20–90 % SOC window.

4 Results

4.1 Measured solar resource and data screening

Fig. 3(a) shows the daily specific yield of the reference plant P1 together with the days excluded by the screening, and Fig. 3(b) the monthly means. The yield follows the seasonal pattern of the Indo-Gangetic plain: a winter minimum in January (2.90 kWh/kWp/day, with fog and haze), a pre-monsoon maximum in May (5.60 kWh/kWp/day, clearness index 0.91) and strongly variable monsoon months, June

having the largest day-to-day spread (standard deviation 1.83 kWh/kWp/day). Across P1 and the 15 co-located reference meters, $16 \times 270 = 4320$ plant-day slots were expected. Of these, 59 were missing because one 140 kWp installation was commissioned only in March, and a further 458 recorded plant-days were flagged (193 Hampel outliers, 134 plant outages, 66 reading-time shifts, 48 stuck registers, 16 campus-outage plant-days and one physical-range violation), leaving 3803 retained plant-days (Fig. 3(c); Additional file 1: Table S5). The campus outage of 9 July 2026, when 14 of the 16 meters recorded less than 0.05 kWh/kWp, is detected by rule 3. For P1, 257 of the 270 recorded days are retained, a data coverage of 95.2 %; September has 23 valid days of the 27 recorded. Over the retained days the mean P1 yield is 4.13 kWh/kWp/day. Including the 13 flagged days, all of which are physically possible readings, the mean is 4.10 kWh/kWp/day, so the screening raises the period mean by only 0.8 %, a limited effect on the mean rather than a proof that the exclusion is unbiased for every statistic. The 13 excluded P1 days comprise one campus outage (9 July), one plant outage (5 September) and 11 days on which the P1 performance index departed from the median of the co-located meters (Hampel rule), indicating a meter or plant fault rather than weather; eight of them lie above and five below the typical yield of their month, and all are listed with their unaltered meter readings in Additional file 1: Table S3. The reference design [10] was sized with a typical-year PVsyst simulation for a site about 20 km from the campus (28.37° N, 77.32° E). Its PVsyst report gives a specific yield of 3.96 kWh/kWp/day (performance ratio 0.831, plane-of-array insolation 1739.6 kWh/m^2), which corresponds to about 5780 kWh for 4 kWp; the 7635 kWh quoted in [10] for the 4 kW station therefore corresponds to a larger simulated array of about 5.3 kWp, and the specific yield is used here for the comparison. With the monthly PVsyst insolation and performance ratio weighted by the valid days of P1 (Eq. (46)), the typical-year estimate gives 4.11 kWh/kWp/day

for January–September against 4.13 kWh/kWp/day measured (+0.6 %), so the average of these months is reproduced closely. The individual months, however, deviate from −20.7 % (June) to +27.3 % (May) (Fig. 4 and Additional file 1: Table S4), and the seasonal means by −7.3 % (winter), +9.0 % (pre-monsoon) and −3.5 % (monsoon). The typical year therefore overestimates the resource in winter and in the early monsoon, the periods in which the station relies on its battery and on the grid, and underestimates the pre-monsoon surplus. Because 2026 is a single year and the PVsyst weather is a synthetic typical year, these deviations represent year-to-year and local variability that a typical-year design cannot capture rather than an error of PVsyst; they are the main motivation for driving the station model with measured data.

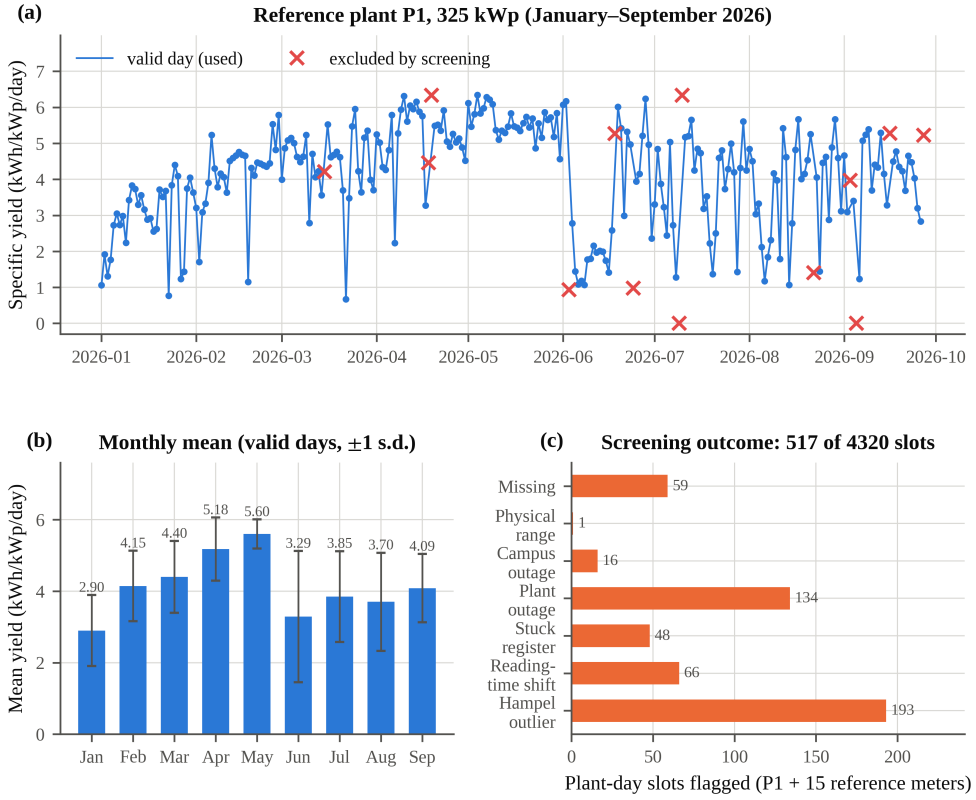


Fig. 3 Reference plant P1 data: (a) daily specific yield with excluded days, (b) monthly mean yield of the valid days, (c) screening outcome by rule for P1 and the 15 co-located reference meters.

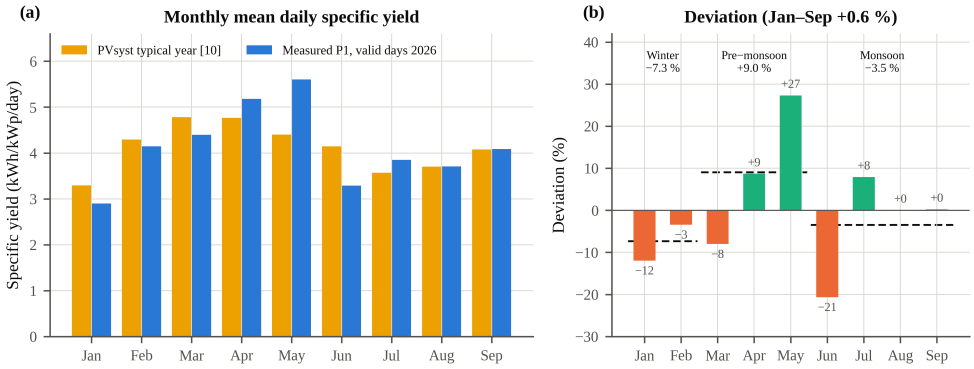


Fig. 4 Matched-period comparison of the measured specific yield of P1 with the typical-year PVsyst estimate of the reference design [10]: (a) monthly mean daily specific yield (measured: valid days of 2026), (b) monthly deviation with seasonal means (dashed).

The co-located reference meters have mean valid-day yields of 0.96–3.76 kWh/kWp/day (Additional file 1: Fig. S3), below the 4.13 kWh/kWp/day of P1, because several older rooftop installations are affected by shading, orientation, soiling and inverter availability. P1, a recently commissioned, unshaded car-park canopy with the most complete record, is therefore the single reference plant of this study. This spread is consistent with performance surveys of rooftop PV in India [21] and means that the station results represent a well-maintained, unshaded array (see Limitations).

4.2 Irradiance reconstruction, PV energy consistency and MPPT

Fig. 5 shows reconstructed plane-of-array irradiance for the highest-, median- and lowest-yield days of the representative winter, pre-monsoon and monsoon months. Clear days follow the clear-sky envelope with peaks of about 830 W/m^2 in January, 1060 W/m^2 in May and 970 W/m^2 in August. In January and May the median day is still a clear-sky profile scaled by haze, whereas in August even the median day (4.15 kWh/kWp) carries strong cloud variability, and the lowest-yield days of January (0.77 kWh/kWp, fog) and August (1.07 kWh/kWp, rain) remain below 500 W/m^2. Table 4

and Fig. 6 compare the PV energy delivered to the DC bus by the Simulink model with the P1 plant energy scaled by capacity to 4 kWp (Eq. (1)). Over the nine months, the model yields 4152.7 kWh against 4248.5 kWh measured, an NMBE of −2.25 % and a monthly CV(RMSE) of 3.30 %; the daily CV(RMSE) is 3.17 %. The individual months lie between +1.47 % (January) and −5.52 % (June). Because the irradiance is scaled to the measured daily yield, this agreement confirms the consistency of the reconstruction, the single-diode model, the temperature model and the converter losses, but it is not an independent validation against measured irradiance. The slightly negative deviation in the hot months arises from the temperature coefficient of the single-diode model (cell temperatures above 60 °C) and from the larger diffuse fraction during the monsoon, which the clear-sky-based reconstruction represents with a fixed diffuse fraction.

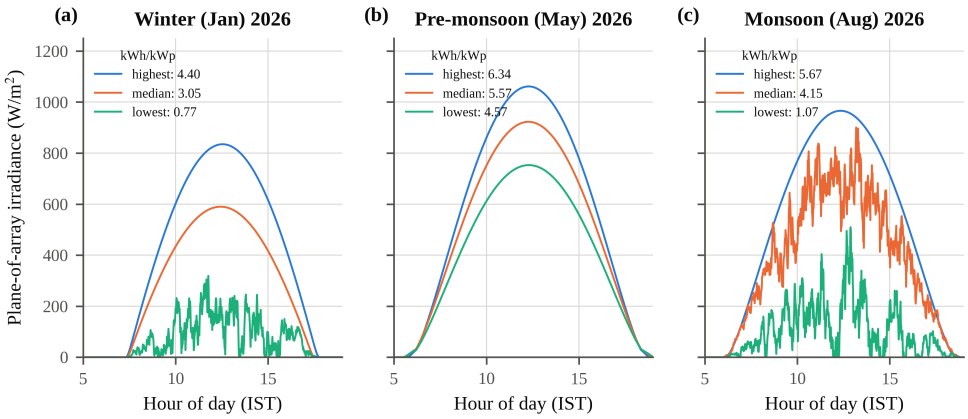


Fig. 5 Reconstructed plane-of-array irradiance for the highest, median and lowest yield days of the representative months: (a) winter (January), (b) pre-monsoon (May), (c) monsoon (August) 2026.

The P&O tracker captured 4268.1 kWh of the 4273.6 kWh available at the maximum power point, a tracking efficiency of 99.75–99.93 % in every month (99.87 % overall), consistent with P&O performance reported in [20, 40]. The reconstructed profiles do not contain the fast irradiance transients of real cloud edges, so this value

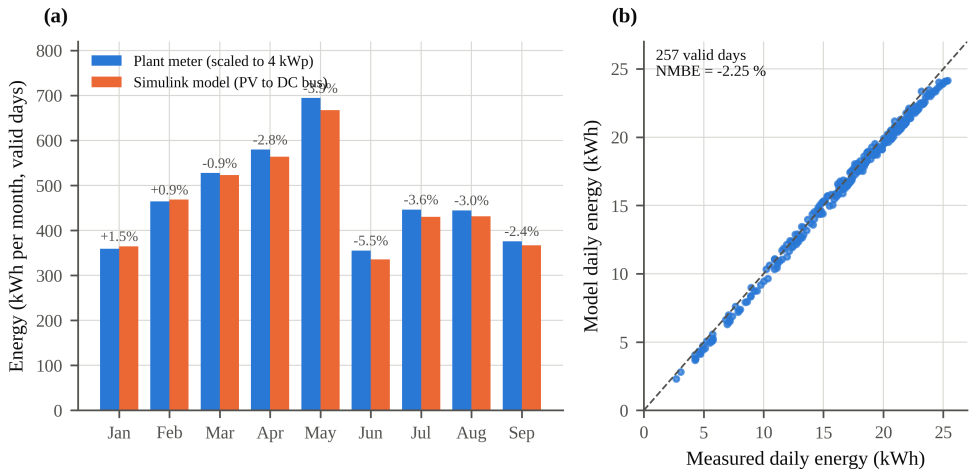


Fig. 6 PV energy consistency check: (a) monthly measured and simulated energy with monthly deviation, (b) daily simulated versus measured energy for the 257 valid days.

Table 4 Monthly PV energy: measured reference-plant energy scaled to 4 kWp and Simulink model (valid days).

Month	Valid days	Measured (kWh)	Model, PV to bus (kWh)	NMBE (%)	Daily CV(RMSE) (%)	MPPT efficiency (%)
Jan	31	359.5	364.8	+1.47	2.33	99.90
Feb	28	464.4	468.8	+0.93	1.23	99.88
Mar	30	527.8	523.1	−0.90	0.99	99.92
Apr	28	579.9	563.9	−2.77	2.90	99.79
May	31	694.6	667.7	−3.86	3.95	99.90
Jun	27	355.2	335.6	−5.52	5.69	99.75
Jul	29	446.5	430.6	−3.57	3.64	99.89
Aug	30	444.5	431.3	−2.98	3.05	99.88
Sep	23	376.0	367.0	−2.37	2.44	99.93
Jan–Sep	**257**	**4248.5**	**4152.7**	**−2.25**	**3.17**	**99.87**

describes tracking under the reconstructed profiles; it is not directly comparable with hardware measurements such as the 98.7 % reported by Vendoti et al. [58]. The fractional-open-circuit-voltage start each morning avoids the dawn tracking delay of a fixed-step P&O, and the power-limiting mode reduced curtailment to 2.55 kWh over nine months (0.06 % of the PV energy).

4.3 Station energy balance and energy contribution

Table 5 and Fig. 7 summarise the monthly energy flows under the rule-based strategy S1, and Fig. 8 shows the energy contributions over January–September. The station delivered 2914.2 kWh to the vehicles (3028.1 kWh at the DC bus). Of the DC-bus EV energy, 2232.0 kWh (73.7 %) came directly from PV, 694.9 kWh (22.9 %) from the BESS and only 101.1 kWh (3.3 %) from the grid (Fig. 8(a)), giving a local energy share of 96.7 %. Of the 4152.8 kWh PV energy at the bus, 53.7 % supplied the vehicles directly, 19.2 % charged the BESS and 27.0 % was exported (Fig. 8(b)). From February to May and in July and September the vehicles were supplied entirely from PV and the BESS, with grid import below 0.1 kWh per month, while January (26.6 kWh) and the monsoon month of June (59.9 kWh) required grid support. The PV energy surplus in spring and summer was exported, with 1053.8 kWh delivered to the grid in nine months, 275.1 kWh of it in May alone. Fig. 7(b) shows that the BESS share of the charging energy is largest in January, July and August, when morning PV is often insufficient for the arrival peak, and that the grid share is largest in June.

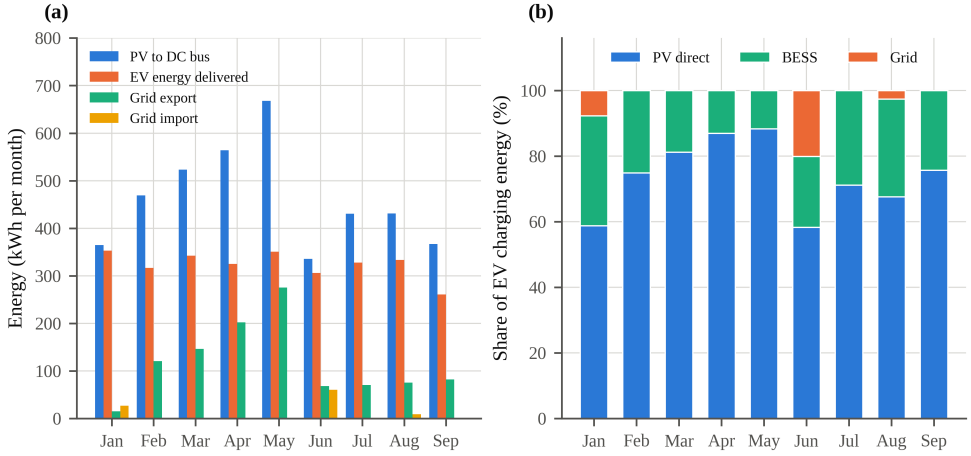


Fig. 7 Monthly energy flows under strategy S1: (a) PV, EV, export and import energy, (b) sources of the EV charging energy.

Table 5 Monthly station energy and service, strategy S1 (valid days).

Month	EV delivered (kWh)	BESS charge / discharge (kWh)	Export (kWh)	Import (kWh)	Local share of EV energy (%)	EVs fully charged	BESS cycles	Station efficiency (%)
Jan	352.7	133.6 / 122.8	14.8	26.6	92.3	348 / 348	5.9	91.8
Feb	316.4	94.6 / 82.5	120.5	0.0	100.0	312 / 312	4.1	91.9
Mar	342.0	78.7 / 66.8	146.4	0.0	100.0	336 / 336	3.4	92.0
Apr	324.8	55.1 / 44.1	202.3	0.1	100.0	318 / 318	2.3	92.2
May	350.4	53.4 / 42.5	275.1	0.1	100.0	342 / 342	2.2	92.2
Jun	306.0	77.7 / 68.9	67.8	59.9	80.0	300 / 300	3.4	92.6
Jul	327.6	113.2 / 98.0	70.3	0.1	100.0	324 / 324	4.9	91.2
Aug	333.5	116.6 / 103.1	75.0	8.5	97.4	330 / 330	5.1	91.4
Sep	260.8	74.6 / 65.8	81.7	0.0	100.0	258 / 258	3.3	91.7
Jan–Sep	**2914.2**	**797.6 / 694.5**	**1053.8**	**95.3**	**96.7**	**2868 / 2868**	**34.6**	**90.9**

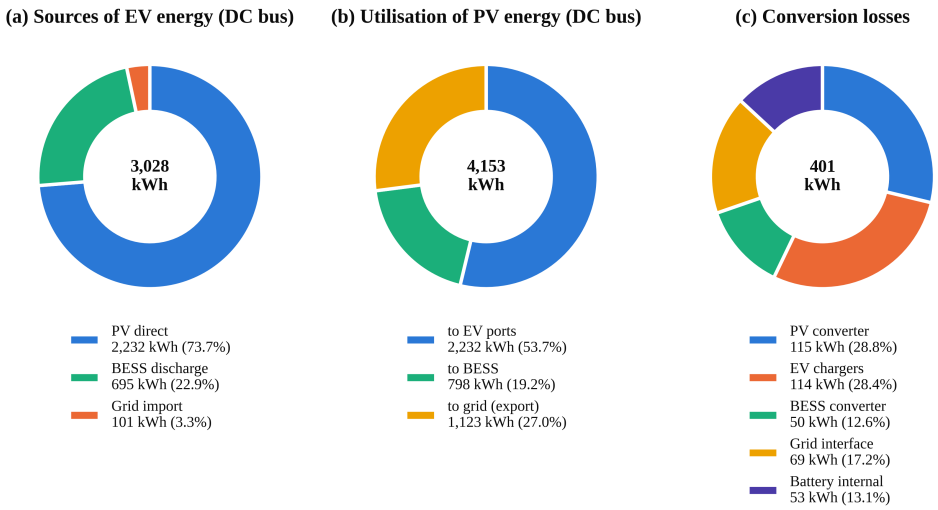


Fig. 8 Energy contribution over January–September 2026 (S1): (a) sources of EV energy, (b) utilisation of PV energy, (c) conversion losses.

The local share in the monthly columns attributes BESS discharge to PV in proportion to the PV fraction of the BESS charge. The DC-bus energy balance closes to better than 0.001 % in all 27 monthly simulations. In the post-processing ledger, allocating the PV and EV energy to their sources leaves residuals of +0.10 and −0.15 kWh (below 0.005 % of the totals), which arise from component-level rounding and from aggregating the 1 s energy meter into one-minute logs; the ±0.5 kWh tolerance used for these checks is an accounting-closure tolerance, not a measurement-accuracy claim. Conversion losses total 401.4 kWh (Fig. 8(c)): PV converter 115.4 kWh (28.8 %), EV chargers 113.9 kWh (28.4 %), grid interface 69.0 kWh (17.2 %), battery internal resistance 52.6 kWh (13.1 %) and BESS converter 50.4 kWh (12.6 %). The overall station efficiency, Eq. (44), is 90.9 % (91.2–92.6 % monthly), in line with MOSFET-based charging stations [7, 32]. The BESS completed 34.6 equivalent full cycles in 257 valid days (0.13 cycles per valid day), where an equivalent full cycle is the DC-bus charge-plus-discharge energy throughput of the BESS divided by twice its nominal energy (2×21.6 kWh), evaluated from the one-minute logged BESS power (34.5 cycles

with the 1 s energy meter); this is well within LFP cycle-life capability. This light cycling does not mean that the battery is oversized: the seasonal results below show that the battery supplies 26–30 % of the vehicle energy in winter and monsoon, and the sensitivity study shows that halving it raises the January grid import by 71 %.

4.4 Seasonal performance

Table 6 and Fig. 9 group the valid days into the three seasons covered by the record. The pre-monsoon season has the highest and most stable resource, 5.06 kWh/kWp/day (95 % block-bootstrap interval 4.74–5.38), while winter (3.49; 3.07–3.93) and monsoon (3.72; 3.29–4.08) give about 30 % less energy per day (Fig. 9(a)). The pre-monsoon interval does not overlap the winter or monsoon interval for any block length between 3 and 14 days, so the seasonal difference is robust to the serial correlation of consecutive days. September is incomplete in the record and October–December are not covered, so the comparison refers to the available record only. The cause differs: in winter the days are short and fog and haze attenuate the beam irradiance, whereas in the monsoon the days are long but cloud and rain make the yield strongly variable (Fig. 5(c)).

The seasons also differ in how the energy is used. In the pre-monsoon season PV alone covers 85 % of the vehicle energy at the bus, the battery is needed only for the early-morning arrivals, grid import is negligible (0.1 kWh in three months) and 38 % of the PV energy is exported (Fig. 9(b), (c)). In winter and monsoon PV covers only about two-thirds of the vehicle energy directly, the battery supplies 30 % (winter) and 26 % (monsoon), and the remaining grid import (26.6 and 68.6 kWh) is concentrated on fog and rain days. The monsoon season, not winter, therefore requires the largest absolute grid support and the largest battery throughput, because it combines low-yield days with long runs of consecutive cloudy days. These seasons determine the battery and grid-interface rating of the station, whereas the pre-monsoon season

Table 6 Seasonal performance of the station, strategy S1 (valid days; seasons after the India Meteorological Department [67]).

Quantity	Winter (Jan–Feb)	Pre-monsoon (Mar–May)	Monsoon (Jun–Sep)	Jan–Sep
Valid days	59	89	109	257
Mean yield (kWh/kWp/day)	3.49	5.06	3.72	4.13
95 % block-bootstrap interval, 7-day blocks (kWh/kWp/day)	3.07–3.93	4.74–5.38	3.29–4.08	—
Independence-based 95 % half-width, descriptive (kWh/kWp/day)	±0.30	±0.20	±0.27	—
PV energy at DC bus (kWh)	833.6	1754.7	1564.6	4152.7
PV energy at DC bus per day (kWh/day)	14.1	19.7	14.4	16.2
EV energy delivered (kWh)	669.1	1017.2	1227.9	2914.2
BESS discharge to EVs (kWh)	205.4	153.4	336.1	694.9
Grid import (kWh)	26.6	0.1	68.6	95.3
Grid export (kWh)	135.2	623.7	294.8	1053.8
PV exported (share of PV at bus)	17.2 %	37.8 %	20.1 %	27.0 %
Local (PV + BESS) share of EV energy	95.9 %	100.0 %	94.3 %	96.7 %

determines the export capacity. A design evaluated with a long-term average or with a single clear-sky day, as in the reference design [10], does not show this difference.

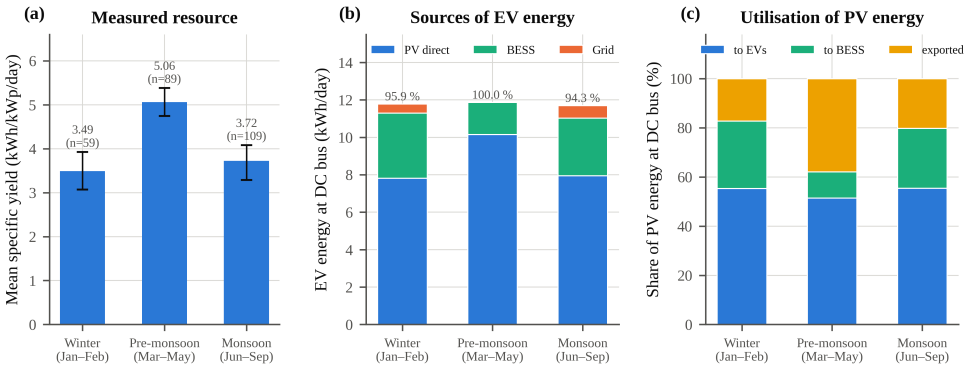


Fig. 9 Seasonal performance (S1): (a) mean daily specific yield with 95 % moving-block bootstrap interval (7-day blocks) and number of valid days, (b) daily sources of EV energy at the DC bus with local share, (c) utilisation of PV energy at the DC bus.

4.5 Daily operation and operating modes

Fig. 10 shows the median days of the representative winter (January, 3.05 kWh/kWp), pre-monsoon (May, 5.57 kWh/kWp) and monsoon (August, 4.15 kWh/kWp) months, selected by the yield-ranking rule described in the data-screening subsection. In winter the morning PV first charges the BESS; when four e-bikes charge simultaneously around 10:00 (3.3 kW), the BESS discharges until the limiter de-rates it near 20 % SOC, and the remaining demand is imported. In the afternoon, surplus PV recharges the BESS to about 37 %. In the pre-monsoon season the BESS reaches the 90 % limit before noon; the limiter then blocks further charging and the surplus is exported at up to 2 kW, while the vehicles are supplied directly from PV. On the monsoon day the PV power fluctuates between about 0.8 and 2.8 kW; the battery absorbs these fluctuations, discharges from 89 % to 77 % during the late-morning peak, and recovers to 90 % by 16:30, so no grid import is needed and only 1.1 kWh is exported in the afternoon, although the yield is 25 % below the May median. The RLS-AEKF estimate follows the true SOC within about 2 % in January and is almost indistinguishable from it in May and August. Additional file 1: Fig. S4 gives the share of time in each operating mode. PV→grid export increases from 1 % of the time in January to 26 % in May, and grid→EV operation occurs only in January, June and August. The five modes of the reference design [10] are reproduced under measured solar conditions.

4.6 EV charging service and vehicle categories

Under the assumed stochastic demand scenario, all 2868 e-bike sessions (11.2 EVs per day) were charged to the 95 % target in every month and strategy, with no unmet energy (Fig. 11). Each session delivered on average 1.016 kWh, in agreement with $30\ Ah \times (0.95 - 0.30) \times 52\ V \approx 1.01$ kWh, and lasted 1.19–1.59 h (mean 1.39 h) including the CV phase (Fig. 11(a), (b)). 90.3 % of the vehicles found a free port on arrival; the mean waiting time was 2.1 min and the longest 72.7 min, during the

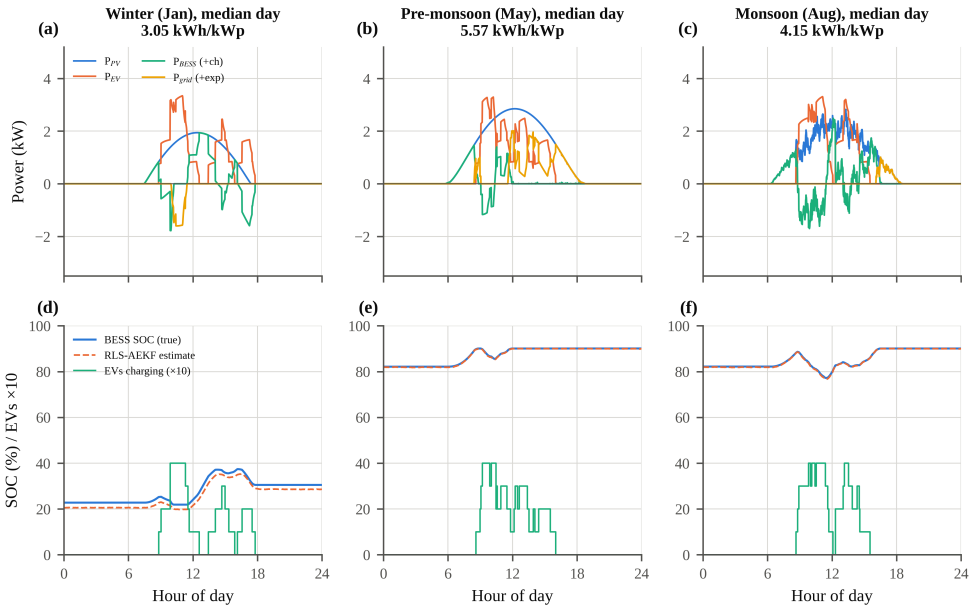


Fig. 10 Median-day operation under S1 in (a, d) winter (January), (b, e) pre-monsoon (May) and (c, f) monsoon (August): (a–c) power flows; (d–f) BESS SOC, RLS-AEKF estimate and number of charging EVs.

morning peak (Fig. 11(c)). Because the demand is assumed, these figures describe the capability of the station for this demand level and do not establish field performance under measured arrival and dwell-time distributions; the sensitivity study shows how they change at higher demand.

The capability of the station for the vehicle classes of Table 3 is shown in Additional file 1: Fig. S5. The number of solar-only charges per day is $\lfloor 0.9\, E_{pv,bus,d}/E_{charge} \rfloor$ with the simulated monthly PV energy per day, and the charging time follows from the 0.8 kW port rating. On solar energy alone the station supports 10 e-bike charges per day in January and 18 in May, 5–10 e-scooter charges, 2–5 e-rickshaw charges and 2–4 e-auto charges, and the four ports can serve about 30 e-bike charges per 10 h day. The 4 kWp station is therefore best suited to two-wheelers, with e-rickshaws and e-autos feasible as a share of the fleet. In the mixed-fleet simulation (8 e-bikes, 3 e-rickshaws and 1 e-auto per weekday, sensitivity study), 97.7 % of the vehicles were

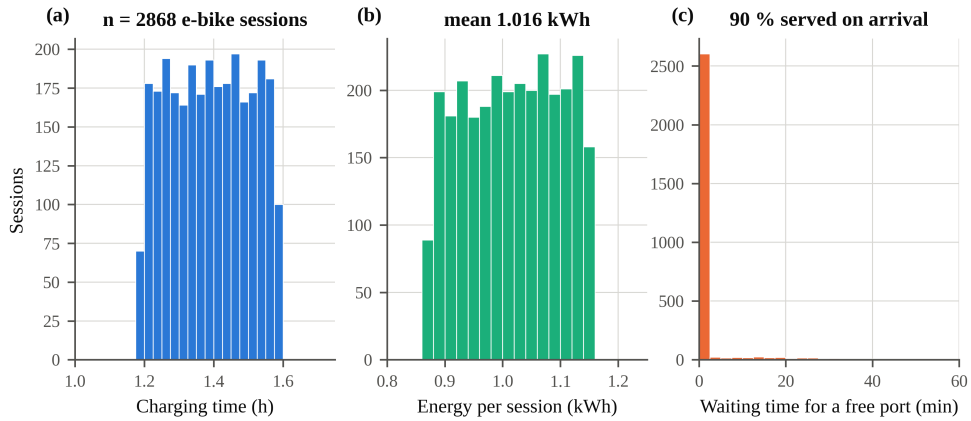


Fig. 11 E-bike charging service, January–September (S1): (a) charging time, (b) energy per session, (c) waiting time for a free port.

fully charged; the remaining sessions were e-autos whose 5.3 h charge occasionally exceeded the dwell time after queuing. A four-wheeler requires a 3.3 kW AC charger and more energy than the station produces on a winter day (0–1 solar-only charges per day), so passenger cars are outside the scope of a 4 kWp design.

4.7 BMS: SOC estimation and SOC window

Fig. 12 shows the four estimators over January, the most demanding month, in which the SOC swings across the full window. Coulomb counting retains its initial error and drifts with the current-sensor bias (0.1 A integrates to about 16 % SOC per month). The EKF and UKF converge quickly but keep a bias of 2–5 % on the OCV plateau and show error spikes of up to 13 % at current steps, because their model resistance is 30 % too high and a 60 A step produces a 0.14 V voltage error that the filter attributes to SOC. The proposed RLS-AEKF identifies the resistance online, from the initial 10.4 mΩ to 8.4 mΩ within the first day (Fig. 12(c)), and learns the OCV offset when the SOC passes the steep ends of the OCV curve; after convergence its error stays within ±1 %.

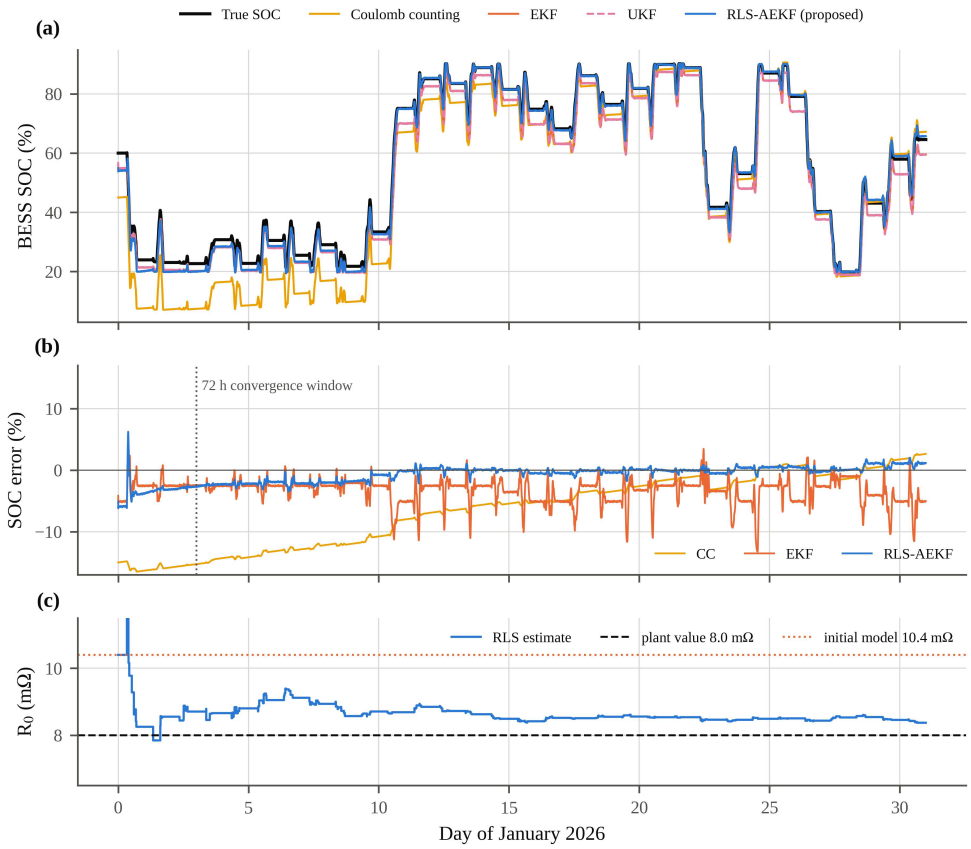


Fig. 12 SOC estimation in January 2026: (a) true SOC and estimates, (b) estimation errors, (c) online RLS identification of the ohmic resistance.

Table 7 SOC estimation accuracy after the 72 h convergence window (simulation, S1, January–September).

Estimator	RMSE range (%)	Mean RMSE (%)	Maximum error range (%)	Online R_0 (mΩ)
Coulomb counting	6.02–8.80	6.95	11.70–15.28	—
EKF	2.43–3.94	3.16	5.63–13.23	fixed 10.4
UKF	2.43–3.94	3.16	5.64–13.24	fixed 10.4
RLS-AEKF (proposed)	**0.25–1.16**	**0.58**	**1.12–4.86**	**7.68–8.37 (plant 8.0)**

Table 7 and Fig. 13 summarise the nine months. The proposed estimator has the lowest RMSE in every month, 0.25–1.16 % (mean 0.58 %), against 3.16 % for the EKF and UKF and 6.95 % for Coulomb counting. Its maximum error is 1.12–4.86 %, against 5.6–13.2 % for the EKF, and the identified resistance lies within 4.7 % of the plant value. The convergence time to a 2 % error band ranged from 13 h (May) to 30 days (January). The long January convergence follows from the operating pattern: in winter the battery operates mostly on the flat part of the LFP OCV curve at low SOC and rarely reaches the steep regions above 90 % or below 20 %, where the OCV offset becomes observable; in May the battery reaches the 90 % limit daily and the offset is learned within hours. These results are obtained in simulation with exact knowledge of the true SOC and quantify the robustness of the estimators to the stated model and sensor errors. Lu et al. [57] reported a maximum error below 2 % for a PSO-tuned adaptive EKF on 25–27 Ah LFP cells under laboratory profiles; experimental confirmation of the present estimator on cells is part of the future work.

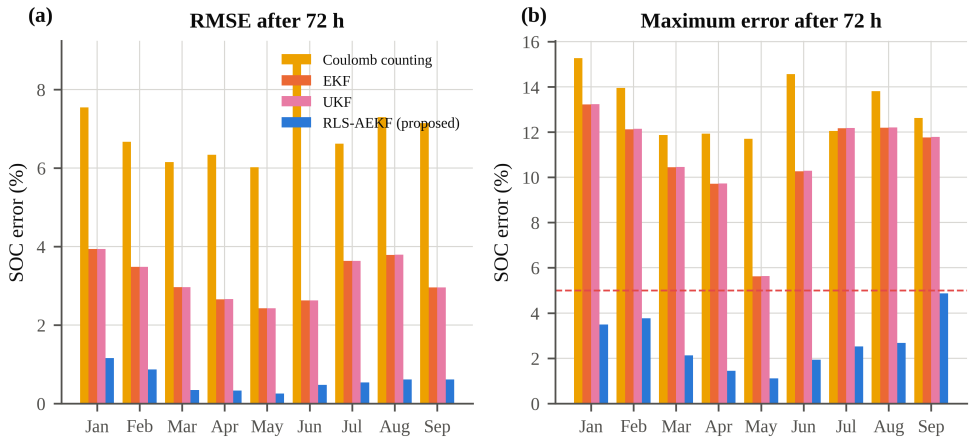


Fig. 13 Monthly SOC estimation accuracy after 72 h: (a) RMSE, (b) maximum error.

The BMS limiter acts on the estimated SOC. Fig. 14(a) shows the charge-power limit falling to zero at 90 % in January, and Fig. 14(b) the distribution of the true SOC over all nine months after the convergence window, which lies within 19.4–90.8 %. The

excursions beyond the nominal limits remain within the 1 % estimation accuracy of the RLS-AEKF and well inside the 5–95 % hard protection, compared with 18.3–92.1 % obtained with an EKF-based BMS without the limiter.

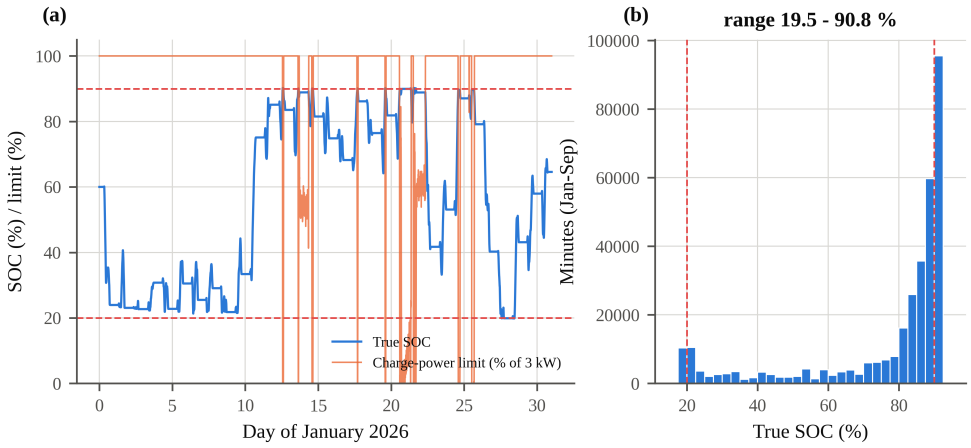


Fig. 14 BMS SOC window: (a) true SOC and charge-power limit in January, (b) distribution of true SOC, January–September.

4.8 DSP forecasting and energy management

Fig. 15 compares the day-ahead predictors on the 257 valid days. RLS achieves the lowest RMSE, 1.136 kWh/kWp/day, 10.5 % below persistence (1.270) and better than the 7-day mean (1.209), LMS (1.201) and NLMS (1.190); its skill score relative to the climatological variance is 16.1 %. The modest absolute skill reflects the inherent difficulty of predicting daily solar energy from past yields alone during the monsoon, when consecutive days are weakly correlated (Fig. 15(a)).

The EMS results are given in Table 8 and Fig. 16. All three strategies charge every vehicle fully. In the months with sufficient solar energy (February–May, July and September) the forecast-based pre-charge is not triggered and S1–S3 coincide. In January, June and August, S2 shifts grid energy to the off-peak period and reduces the monthly cost by Rs 4.2, 10.4 and 0.7 (S3: Rs 13.1, 31.6 and 4.7). Over nine months

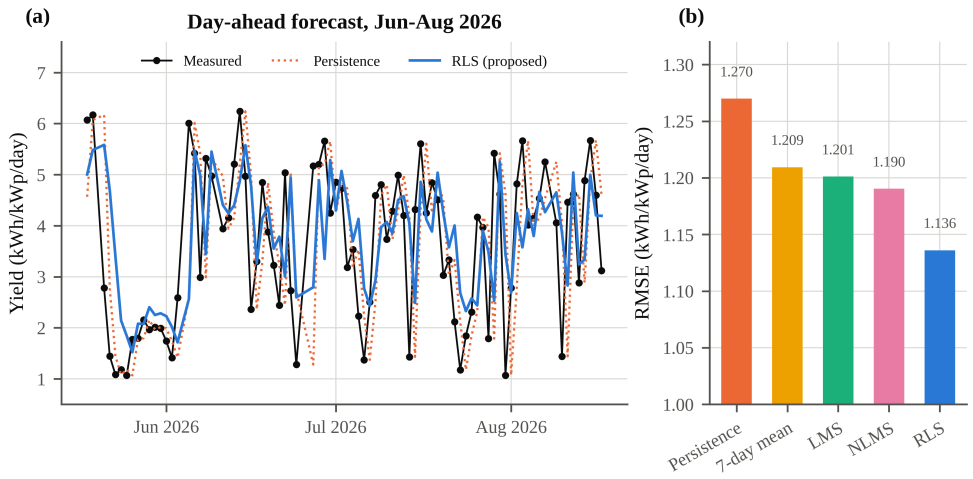


Fig. 15 Day-ahead PV forecasting: (a) measured yield and RLS and persistence forecasts, June–August, (b) RMSE of the predictors.

Table 8 Energy management strategies, January–September (valid days).

Quantity	S1 rule-based	S2 RLS forecast	S3 perfect forecast
Grid import (kWh)	95.3	99.8	102.3
Off-peak import, 22:00–06:00 (kWh)	0.0	39.8	94.0
Peak import, 18:00–22:00 (kWh)	1.05	1.05	0.53
Grid export (kWh)	1053.8	1055.3	1053.5
Net energy cost (Rs)	−2492.6	−2507.9	−2542.1
Saving relative to S1 (Rs)	—	15.3	49.4
Local share of EV energy (%)	96.7	97.9	99.7
BESS equivalent cycles	34.6	36.4	39.0
Grid-only station cost (Rs)	22417	22417	22417

S2 reduces the operational net energy cost by Rs 15.3, about 0.61 % of its absolute value, and even perfect forecasting (S3) reduces it by only Rs 49.4 (2.0 %), while both add 1.8–4.4 equivalent battery cycles. The forecast improvement (10.5 % lower RMSE) is therefore real, but its monetary effect is small at this station. With a local energy share of 96.7 % already achieved by the rule-based strategy and the assumed tariff spread, forecast-based pre-charging therefore has a small economic effect at this station; its effect is concentrated in cloudy and monsoon periods and would grow with

a larger peak/off-peak tariff spread or a higher demand, in agreement with the EMS classifications in [4, 16]. The forecast-uncertainty margin m ensures that S2 never costs more than S1. The tariff scenarios below show that a wider peak/off-peak spread raises the S2 saving about fivefold.

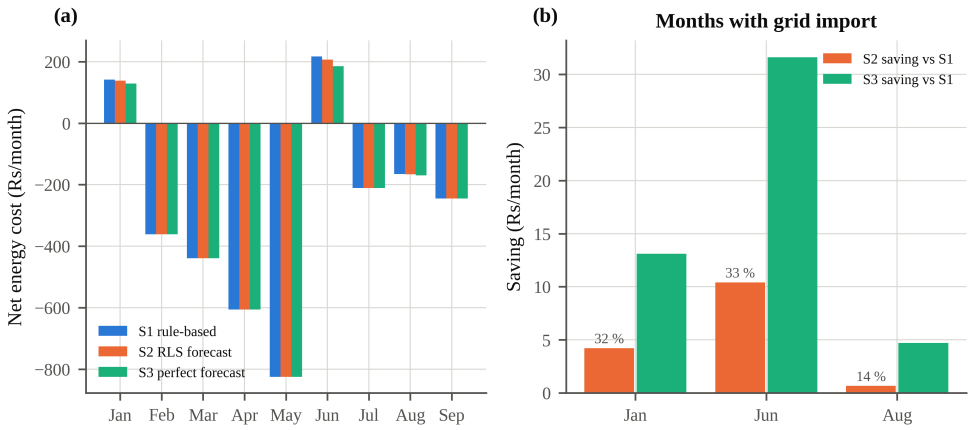


Fig. 16 Energy management comparison: (a) monthly net energy cost of S1, S2 and S3, (b) savings in the months with grid import.

4.9 Power quality of the grid interface

The grid-current indices from the switching model are summarised in Table 9 and Figs. 17–18. With an undistorted grid, the MOSFET-based three-level T-type inverter with LCL filter gives a TDD of 0.69–1.01 % at all power levels and a THD of 1.33 % at 3 kW export, so the converter design itself stays well below the 5 % comparison line derived from IEEE 519 [43]. With the assumed 3 % third- and 2 % fifth-harmonic grid-voltage distortion and fundamental feed-forward only, the third and fifth current harmonics reach 6.4 % and 4.2 % of the fundamental at 3 kW, the THD rises to 7.61 % and the TDD to 5.22–5.72 %, which exceeds the 5 % comparison line at all power levels. The conventional multi-resonant PR+HC benchmark reduces the THD at 3 kW to 1.24 % and the TDD to 0.65–0.97 % at all power levels. The proposed RLS

harmonic estimator reduces the THD at 3 kW from 7.61 % to 1.74 % (a 77 % reduction) and the TDD to 0.77–1.29 %, with a power factor of 0.998 at rated power. Both harmonic-control methods therefore bring the TDD well below the 5 % comparison line (assumed I_L). At 3 kW the individual harmonics with RLS compensation are 1.17 % (3rd), 0.61 % (5th) and 0.13 % (7th) of the fundamental, far below the 4 % individual-harmonic comparison line. Ranked by steady-state distortion, the multi-resonant PR+HC benchmark performs best (THD 1.24 %, TDD $\leq$ 0.97 %), and the RLS estimator second (THD 1.74 %, TDD $\leq$ 1.29 %). The RLS method is therefore presented as an adaptive candidate rather than the best steady-state controller: it does not need a resonant controller per harmonic and provides online estimates of the grid-voltage harmonic amplitudes (third and fifth harmonic within 7.6 % and 4.2 % of the FFT reference), which can be used for power-quality monitoring at the point of common coupling [38, 42]; its advantage under changing grid harmonics and frequency has not been tested here. Because I_L and the short-circuit ratio of the real connection point are unknown and the results are steady-state simulations, they indicate the expected margin; formal IEEE 519 compliance is not inferred.

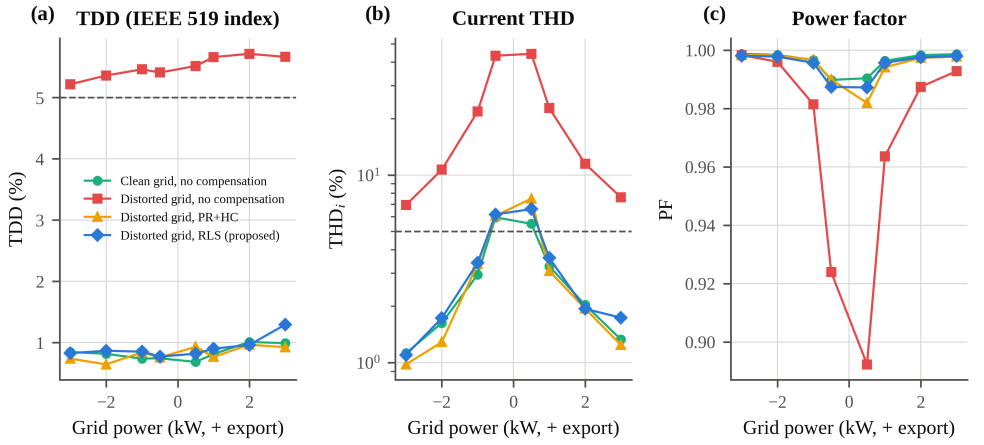


Fig. 17 Grid-current power quality versus grid power for four cases: (a) TDD, (b) THD (logarithmic), (c) power factor. Dashed line: 5 % TDD comparison line (strictest IEEE 519-2022 limit, assumed I_L).

Table 9 Grid-current power quality at rated export (3 kW) and over all power levels (−3 to +3 kW).

Case	THD at 3 kW (%)	TDD at 3 kW (%)	TDD range, all levels (%)	PF at 3 kW	TDD vs 5 % comparison line (assumed I_L = 17.4 A)
Clean grid, no compensation	1.33	0.99	0.69–1.01	0.999	below at all levels
Distorted grid, no compensation	7.61	5.66	5.22–5.72	0.993	above at all levels
Distorted grid, PR+HC benchmark	1.24	0.93	0.65–0.97	0.998	below at all levels
Distorted grid, RLS (proposed)	1.74	1.29	0.77–1.29	0.998	below at all levels

At low power (±0.5 kW) the THD of all methods is about 6 %, because a nearly constant residual harmonic current is divided by a small fundamental (Fig. 17(b)); the TDD, used here as the current-distortion index, remains below 1 % at these points. THD is reported for comparison only and is not the compliance metric. Fig. 18 shows the grid current and its spectrum at 3 kW export: without compensation the third and fifth harmonics dominate, and with RLS compensation all harmonics are below 1 % of the fundamental. When the TDD map is applied to the one-minute grid power of the monthly simulations (Fig. 19), the estimated time-weighted mean TDD is 0.85–0.93 % with RLS compensation against 5.48–5.64 % without it, and the estimated 95th-percentile TDD does not exceed 1.17 % in any month. The grid interface is active for 5 % (January) to 30 % (May) of the time (Fig. 19(b)). These monthly values are estimates obtained by interpolating the steady-state switching results onto the power profile. The hardware PV–fuel-cell–storage charging system of Vendoti et al. [58] reported a current THD of 2.1 %; Verma and Singh [41] also report IEEE 519 compliance with adaptive control.

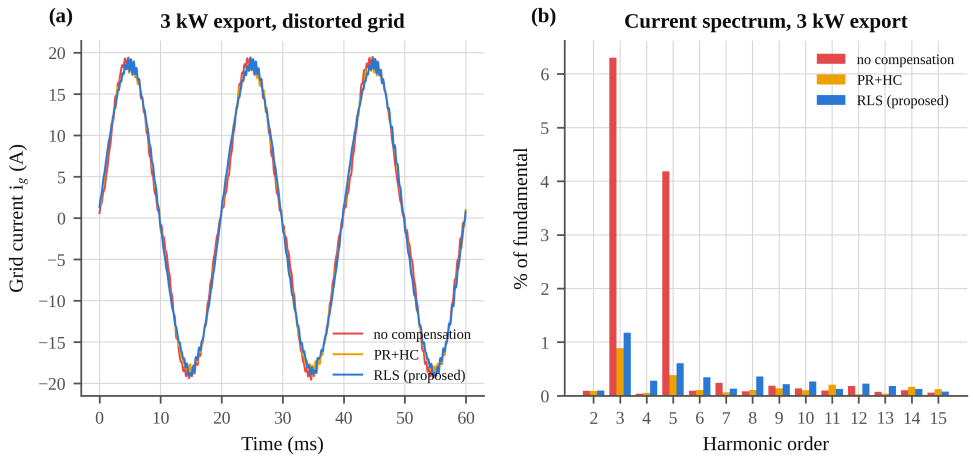


Fig. 18 Grid current at 3 kW export with a distorted grid: (a) waveforms, (b) harmonic spectrum.

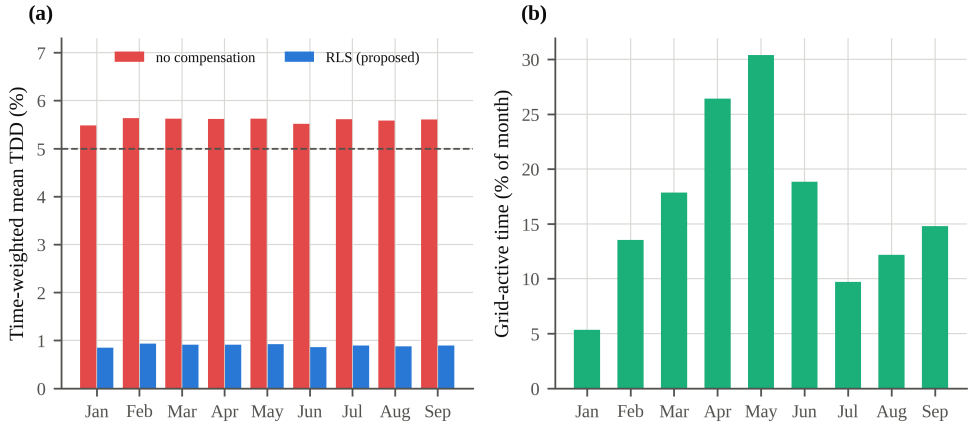


Fig. 19 Estimated monthly time-weighted power quality (S1): (a) mean TDD without and with RLS compensation, (b) share of time with active grid exchange.

4.10 Operational energy cost, emissions, sensitivity and robustness

The economic results are operational energy costs: the cost of grid import minus the export credit. Capital, operation and maintenance, replacement and battery-degradation costs are not included, so the results do not establish economic feasibility. A negative calculated cost denotes a net operational credit after export revenue; it does

not demonstrate project profit, payback or lifecycle economic feasibility. Supplying the same EV energy from the grid alone would cost Rs 22417 under the assumed ToD tariff (about Rs 7.7 per delivered kWh including the 94 % grid-interface efficiency). The PV–BESS station instead has a net operational energy cost of −Rs 2493 over the nine months, i.e. a net operational credit after export revenue, and avoids about 2.05 t of operating CO_2 emissions (Eq. (45) with $EF = 0.727$ kgCO_2/kWh [66]); with an emission factor 10 % lower or higher the avoided emission is 1.84–2.25 t. These are assumed sensitivity bounds, and the embodied emissions of the PV array, battery and converters are excluded.

Because the tariff is assumed, Table 10 recomputes the operational energy cost for other price levels with the simulated energy flows; this is valid because the EMS dispatch depends on time windows and the forecast, not on the price values. The station result depends mainly on the export credit: without any export credit the nine-month cost becomes +Rs 669, still 97 % below the grid-only station. The forecast-based saving of S2 grows from Rs 15.3 to Rs 84.9 when the peak/off-peak spread is widened to ×1.5/×0.6, which confirms that its value depends on the tariff structure rather than on the forecast accuracy alone. These results agree with the techno-economic findings for PV-powered charging under Indian climate conditions in [9, 21].

The sensitivity and robustness results for January, the month with the lowest solar resource, are given in Table 11 and Fig. 20. Halving the BESS to 225 Ah reduces the local share from 92.3 % to 86.7 %, raises the grid import from 26.6 to 45.6 kWh (+71 %) and the monthly cost by 55 %, whereas increasing it to 675 Ah gains only 2.2 percentage points; the 450 Ah capacity of the reference design is therefore a balanced choice for the winter and monsoon seasons, although it is lightly cycled in the pre-monsoon season. Raising the demand to 20 e-bikes per day keeps every session fully charged but reduces the local share to 60.2 %; at 30 e-bikes per day the four ports

Table 10 Operational energy cost (Rs) for January–September under tariff scenarios (energy flows of the simulations unchanged).

Scenario	Base price (Rs/kWh)	Peak / off-peak multiplier	Export credit (Rs/kWh)	S1	S2	S3	S2 saving	Grid-only station
Low prices	6.0	1.20 / 0.85	2.0	−1534	−1547	−1577	12	19215
Base (assumed)	7.0	1.20 / 0.85	3.0	−2493	−2508	−2542	15	22417
High prices	8.0	1.20 / 0.85	4.0	−3451	−3469	−3507	18	25620
No export credit	7.0	1.20 / 0.85	0	669	658	618	11	22417
Wider ToD spread	7.0	1.50 / 0.60	3.0	−2490	−2575	−2706	85	–

become the bottleneck and 90.6 % of the sessions are fully charged. The three intra-day irradiance shapes change the local share by at most 0.48 % and leave EV service unchanged, which indicates that the energy and service conclusions are insensitive to the reconstructed intra-day shape. A change of PR_{ref} by ±0.05 changes the PV energy by about ±6 % and the local share by about ±2 percentage points.

Table 11 Sensitivity and robustness, January 2026 (S1).

Case	PV to bus (kWh)	Local share (%)	Grid import (kWh)	EVs fully charged (%)	Net cost (Rs)
Base: 450 Ah, 12 e-bikes/day, PR_{ref} 0.80	364.8	92.3	26.6	100.0	142
BESS 225 Ah	364.8	86.7	45.6	100.0	220
BESS 675 Ah	364.8	94.5	18.9	100.0	107
20 e-bikes/day	364.8	60.2	229.7	100.0	1612
30 e-bikes/day	364.8	41.4	497.8	90.6	3552
Mixed fleet (8 e-bike, 3 e-rickshaw, 1 e-auto)	364.8	55.7	279.0	97.7	1956
Irradiance shape: smooth	365.0	92.5	26.0	100.0	139
Irradiance shape: high variability	362.8	92.1	27.1	100.0	151
Irradiance shape: morning-skewed	365.0	92.7	25.0	100.0	132
PR_{ref} 0.75	389.9	94.2	20.1	100.0	53
PR_{ref} 0.85	342.6	90.3	33.6	100.0	226

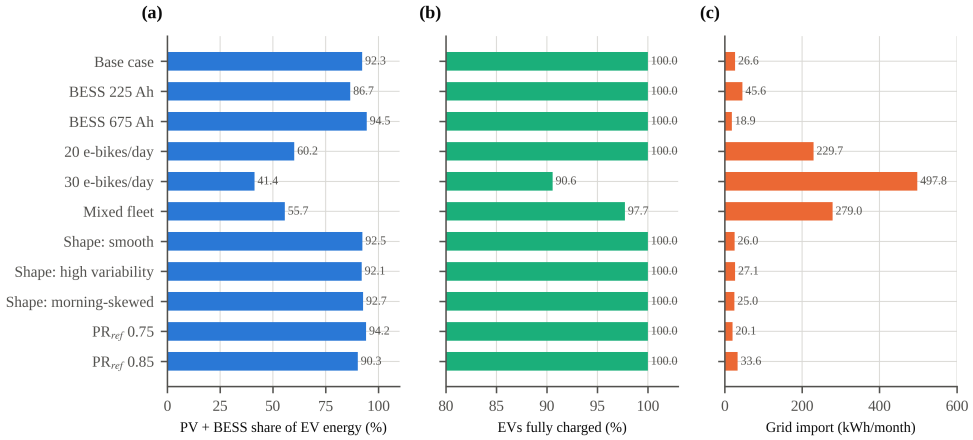


Fig. 20 Sensitivity and robustness in January: (a) PV + BESS share of EV energy, (b) EVs fully charged, (c) grid import.

5 Discussion

5.1 Comparison with the reference design and published studies

Table 12 compares the present work with the reference design and two recent studies.

The main differences from the reference design are the measured solar input over nine months reported by season, the dual-timescale modelling, the BMS with SOC estimation error and limiter, the grid interface assessed with THD and TDD over all power levels, the tariff-scenario analysis and the vehicle-class analysis. The results of Vendoti et al. [58] and Lu et al. [57] are hardware and laboratory results, whereas the corresponding results of this work are simulation results; the comparison therefore shows the level reached, not an equivalence of evidence.

5.2 Implications for station design and energy management

The results connect the station-level behaviour to recent data-driven studies of EV charging. Xu et al. [68] and Hao [69] show that charging scheduling and charging demand shape the clean-energy supply and control of regional grids. At the scale of a single 4 kWp station the same effect appears in the seasonal grid exchange: winter and monsoon account for 95.2 of the 95.3 kWh of grid import, whereas the pre-monsoon season exports 38 % of its PV energy. Zheng and Zheng [70] optimise the layout of charging facilities to raise renewable-energy consumption; the seasonal local shares of 94.3–100 % found here indicate that a light-EV station sized for the winter and monsoon resource consumes most of its PV energy locally, and that the pre-monsoon surplus is an opportunity for additional demand or export. Ostermann and Haug [71] show that the value of charging-demand forecasts depends on the aggregation level and the energy-procurement setting. Consistent with this, the day-ahead PV forecast of this work lowered the forecast error by 10.5 % but changed the operational energy

Table 12 Comparison with the reference design and published studies.

Aspect	Singla et al. [10]	Vendoti et al. [58]	Lu et al. [57]	This work
Solar input	PVsyst estimate, constant irradiance	test conditions	—	measured campus data, 257 days, screened per IEC 61724-1
Simulation horizon	seconds (mode demonstration)	seconds	laboratory test profiles	9 months at 1 s (system) + 1 μs switching (converter)
Seasonal analysis	none	none	—	winter, pre-monsoon, monsoon
Mean daily specific yield	PVsyst 3.96 kWh/kWp/day (typical year); 4.11 for Jan–Sep	—	—	4.13 kWh/kWp/day measured, Jan–Sep (+0.6 %); months −21 % to +27 %
Switching devices	diodes	—	—	MOSFET synchronous converters
MPPT efficiency	not reported	99.5 % sim., 98.7 % hardware	—	99.75–99.93 % (reconstructed irradiance)
Grid current distortion	not reported	THD 2.1 % (hardware)	—	PR+HC THD 1.24 %; RLS THD 1.74 %, TDD $\leq$ 1.29 % (simulation)
SOC estimation	not modelled	—	PSO-tuned adaptive EKF, max. error $<$ 2 % (LFP cells)	RLS-AEKF, RMSE 0.25–1.16 % (simulation, model mismatch)
Energy management	five fixed modes	rule-based	—	five modes + RLS forecast + perfect-forecast benchmark
EV classes	e-bike	—	—	e-bike, e-scooter, e-rickshaw, e-auto
Economics and CO_2	not reported	not reported	—	operational energy cost, tariff scenarios, CO_2 range

cost of a single station by only 0.61 % under the assumed tariff, and its value grew about fivefold with a wider peak/off-peak spread (Table 10). For station planners, three practical points follow: measured multi-season data rather than a typical-year estimate should set the battery and grid-interface ratings; the battery is lightly cycled on average (0.13 equivalent cycles per valid day) but is needed in the low-resource seasons; and forecast-based scheduling is most useful where tariff spreads or demand are larger or where several stations are aggregated.

5.3 Assessment of the evidence

Table 13 lists the assessment criteria, the study targets, the results and the strength of each conclusion. The outcome column separates targets met in simulation, results that hold only for an assumed scenario, and comparison lines from which no formal compliance is inferred.

5.4 Limitations

The study has the following limitations. (i) The measured data are daily energies; the one-minute irradiance is reconstructed and scaled to the measured daily yield, so the PV energy agreement is a consistency check, and MPPT performance under real cloud transients is not represented. (ii) The study uses one building, the reference plant P1, which is the best-performing, unshaded installation of the campus. A hold-out test that predicted each of the co-located installations from the P1 series met the adopted diagnostic thresholds $|\mathrm{NMBE}| \leq 10$ % and $\mathrm{CV(RMSE)} \leq 30$ % for 7 of 15 plants on weekly totals and 5 of 15 on daily values, because the plants differ in shading, soiling and availability; the energy results therefore apply to a well-maintained, unshaded array, and for a lower-yield site the PV energy scales with the plant yield ratio (0.46–0.81 for the campus plants). The hold-out diagnostic shows that capacity-only scaling from one reference plant does not generalise reliably to the other plants, because local orientation, shading, clipping, curtailment and data-quality effects are

Table 13 Assessment of the evidence: study targets, results and the strength of each conclusion.

Criterion	Target	Result	Outcome
Data coverage of the reference plant after screening	reported	257 / 270 days (95.2 %)	coverage reported; not an IEC compliance determination
PV energy consistency, 9 monthly totals: NMBE / CV(RMSE)	reported	−2.25 % / 3.30 %	consistency check; not an independent validation
MPPT efficiency (reconstructed irradiance)	> 98 % (study target; cf. EN 50530 [62])	99.75–99.93 %	simulation target met; EN compliance not inferred
E-bike sessions fully charged	≥ 99 %	8604 / 8604 (27 simulations)	met in assumed demand scenario
Unmet EV energy	0 kWh	0.000 kWh	met in assumed demand scenario
DC-bus energy closure	< 1 %	< 0.001 %	met (numerical check)
True BESS SOC after 72 h	20–90 % ± 1 %	19.4–90.8 %	simulation target met
RLS-AEKF RMSE after 72 h	< 2 %	0.25–1.16 %	simulation target met
RLS-AEKF maximum error after 72 h	< 5 %	4.86 %	simulation target met
RLS-AEKF lower RMSE than CC, EKF, UKF in every month	lower	0.58 % vs 6.95 / 3.16 / 3.16 %	simulation target met
Online R_0 identification error	< 15 %	4.7 %	simulation target met
RLS forecast vs persistence	lower RMSE	1.136 vs 1.270 kWh/kWp	met
S2 cost ≤ S1 cost	yes	Rs −2508 vs −2493	met in assumed tariff scenario
Mean daily specific yield vs PVsyst, matched months	comparison only	4.13 vs 4.11 kWh/kWp/day (+0.6 %); monthly −20.7 % to +27.3 %	matched-period resource comparison; single measured year
Effect of screening on mean yield	< 2 %	+0.8 %	met
Seasonal difference robust to serial correlation	non-overlapping intervals	pre-monsoon interval separate for 3–14-day blocks	met (block bootstrap)
Robustness to irradiance shape	< 5 % / < 1 point	0.48 % / 0.00 point	met
THD at 3 kW export, RLS	< 5 % (comparison only)	1.74 %	below comparison value; THD is not the compliance metric
Individual harmonics at 3 kW, RLS (3rd, 5th, 7th)	< 4 % comparison line [43]	1.17, 0.61, 0.13 %	below assumed 4 % line; formal IEEE compliance not inferred
TDD, clean grid, all levels	< 5 % comparison line (assumed I_L)	≤ 1.01 %	below assumed 5 % line; formal IEEE compliance not inferred
TDD, RLS, all levels	< 5 % comparison line (assumed I_L)	≤ 1.29 %	below assumed 5 % line; formal IEEE compliance not inferred
TDD, PR+HC benchmark, all levels	reported	≤ 0.97 %	lower steady-state TDD than RLS
Estimated monthly 95th-percentile TDD, RLS	< 5 % comparison line	≤ 1.17 %	estimate below assumed 5 % line

not modelled. (iii) The 4 kWp energy is obtained by capacity scaling of a 325 kWp plant. (iv) The EV demand, the ToD tariff and the grid-voltage distortion are assumed scenarios, and the economic results exclude capital and life-cycle costs. (v) SOC estimation and the converter results are simulation results; the power-quality results are steady-state values for an assumed I_L, while the short-circuit ratio of the real connection point is unknown. (vi) The data cover January–September; the post-monsoon season (October–December) is not included, and the seasonal intervals rest on a block bootstrap of 59–109 valid days per season.

6 Conclusions

A 4 kWp PV–BESS–grid charging station for light electric vehicles was assessed with nine months of measured daily energy from an operating 325 kWp car-park canopy PV plant, screened with seven IEC 61724-1-informed and statistical rules without altering any measured value, scaled by capacity, and simulated at 1 s for every valid day together with a 1 μs switching model of the grid interface. The main conclusions are:

1. Over January–September the measured mean daily specific yield (4.13 kWh/kWp/day over 257 valid days) agrees with the typical-year PVsyst estimate of the reference design within 0.6 %, but individual months deviate by -21 % to $+27$ %, and the winter and monsoon seasons lie 7 % and 4 % below the estimate. A single typical-year average therefore hides the seasonal shortfalls that set the battery and grid-support requirement.
2. The seasons differ strongly: the mean yield is 3.49 (winter), 5.06 (pre-monsoon) and 3.72 kWh/kWp/day (monsoon). The pre-monsoon season is supplied almost entirely locally and exports 38 % of the PV energy, whereas winter and monsoon need the battery for 26–30 % of the vehicle energy and account for nearly all grid import; the monsoon season sets the largest grid-support requirement.

3. With the 450 Ah BESS and an assumed demand of 11.2 e-bikes per day, PV supplies 73.7 %, the BESS 22.9 % and the grid 3.3 % of the charging energy; grid support is needed mainly in January and June. The station efficiency is 90.9 %, and 27 % of the PV energy is exported.
4. The proposed RLS-AEKF estimator, with event-triggered resistance identification, OCV-offset augmentation and plateau-aware noise, reduced the mean SOC RMSE to 0.58 % in simulation with deliberate model and sensor errors, and with the SOC limiter kept the battery within 19.4–90.8 %. Independent battery tests or hardware-in-the-loop validation are required before an experimental BMS accuracy can be claimed.
5. Under the assumed grid-voltage distortion, the multi-resonant PR benchmark gave the lowest steady-state distortion (THD 1.24 %), and the RLS harmonic estimator reduced the current THD at 3 kW from 7.61 % to 1.74 % and kept the TDD at or below 1.29 % at all power levels, with the additional benefit of online harmonic estimation; RLS therefore remains a candidate for adaptive compensation whose advantage under time-varying grid conditions is still to be tested. Both stay below the 5 % TDD comparison line in steady-state simulation; formal IEEE 519 compliance cannot be concluded because the short-circuit strength, the I_{SC}/I_L ratio and the duration-based aggregation of the standard at the point of common coupling were unavailable.
6. Day-ahead RLS forecasting reduced the forecast RMSE by 10.5 % relative to persistence, but forecast-based pre-charging changed the nine-month operational energy cost by only 0.61 % because the rule-based strategy already achieves a local share of 96.7 %; its value grows about fivefold with a wider peak/off-peak tariff spread.
7. The station is best suited to two-wheelers (10–18 solar-only e-bike charges per day), can serve e-rickshaws and e-autos as a share of the fleet, and is not suitable for passenger cars.

6.1 Future work

Future work will extend the measured period to a full calendar year to include the post-monsoon season; compare the measured yield with independent satellite irradiance (for example NASA POWER) and obtain minute-resolution irradiance or inverter power data to assess MPPT and EMS behaviour under real cloud transients; record actual charging sessions at the campus to replace the assumed demand scenario; confirm the RLS-AEKF estimator experimentally on LFP cells and a hardware BMS; implement the station controllers on a real-time digital controller with hardware-in-the-loop testing; evaluate the RLS harmonic estimator with measured grid-voltage distortion, the actual short-circuit ratio at the point of common coupling and time-varying harmonic conditions; and include capital and replacement costs, battery ageing and multi-station sizing in a full techno-economic optimisation.

Abbreviations. AEKF, adaptive extended Kalman filter; BESS, battery energy storage system; BMS, battery management system; CC, Coulomb counting; CC-CV, constant current–constant voltage; CI, confidence interval; CV(RMSE), coefficient of variation of the root-mean-square error; DAB, dual active bridge; DSP, digital signal processing; EKF, extended Kalman filter; EMS, energy management system; EV, electric vehicle; FFT, fast Fourier transform; IMD, India Meteorological Department; LCL, inductor–capacitor–inductor filter; LFP, lithium iron phosphate; LMS, least mean squares; MPPT, maximum power point tracking; NLMS, normalised least mean squares; NMBE, normalised mean bias error; NOCT, nominal operating cell temperature; OCV, open-circuit voltage; P&O, perturb and observe; PF, power factor; PLL, phase-locked loop; PR, proportional-resonant; PR+HC, proportional-resonant with harmonic compensators; PV, photovoltaic; PWM, pulse-width modulation; RLS, recursive least squares; RMSE, root-mean-square error; SOC, state of charge; SOGI, second-order generalised integrator; STC, standard test conditions; TDD, total

demand distortion; THD, total harmonic distortion; ToD, time of day; UKF, unscented Kalman filter.

Supplementary information. Additional file 1. Table S1: nomenclature of symbols; Table S2: simulation parameters of the average-value and switching models; Table S3: days of the reference plant excluded by the screening; Table S4: monthly comparison of the measured specific yield with the typical-year PVsyst estimate; Fig. S1: Simulink average-value model; Fig. S2: Simscape switching model; Table S5: capacity history and plant-day accounting of the co-located reference meters; Fig. S3: mean daily specific yield of the co-located reference meters; Fig. S4: share of time in each operating mode; Fig. S5: solar-only charges per day by vehicle class (PDF).

Acknowledgements. The authors acknowledge the host institution for the MATLAB R2026b software environment and for access to the campus PV energy-meter records.

Declarations

Author contributions. A.S.: conceptualization, methodology, modelling and simulation, formal analysis, visualization, writing – original draft. M.R.: supervision, validation, resources, writing – review and editing. S.D.: conceptualization, supervision, validation, writing – review and editing. P.G.: supervision, validation, writing – review and editing. All authors read and approved the final manuscript.

Funding. Not applicable. The authors did not receive support from any organization for the submitted work.

Data availability. The anonymized daily PV energy-meter records, screening flags, simulation models and post-processing scripts are available from the corresponding author on reasonable request, subject to institutional data-sharing permission.

Ethics approval and consent to participate. Not applicable.

Consent for publication. Not applicable.

Competing interests. The authors declare no competing interests.

References

[1] Rivera S, Goetz SM, Kouro S, et al (2023) Charging infrastructure and grid integration for electromobility. Proc IEEE 111(4):371–396. https://doi.org/10.1109/JPROC.2022.3216362

[2] Brenna M, Foiadelli F, Leone C, et al (2020) Electric vehicles charging technology review and optimal size estimation. J Electr Eng Technol 15:2539–2552. https://doi.org/10.1007/s42835-020-00547-x

[3] Leone C, Longo M (2021) Modular approach to ultra-fast charging stations. J Electr Eng Technol 16:1971–1984. https://doi.org/10.1007/s42835-021-00757-x

[4] Bhatti AR, Tamoor M, Liaqat R, et al (2024) Electric vehicle charging stations and the employed energy management schemes: a classification based comparative survey. Discov Appl Sci 6(10). https://doi.org/10.1007/s42452-024-06190-9

[5] Rana R, Saggu TS, Letha SS, et al (2024) V2G based bidirectional EV charger topologies and its control techniques: a review. Discov Appl Sci 6:588. https://doi.org/10.1007/s42452-024-06297-z

[6] Reddy BN, Jyothi B, Rao GS, et al (2026) State-of-the-art DC-DC converters for electric mobility and renewable integration: trends, challenges, and future directions. Discov Appl Sci 8:160. https://doi.org/10.1007/s42452-025-08120-9

[7] Rajendran G, Vaithilingam CA, Naidu K, et al (2020) Energy-efficient converters for electric vehicle charging stations. SN Appl Sci 2:583. https://doi.org/10.1007/s42452-020-2369-0

[8] Tamba JSII, Abdulkarim A, Shuaibu AN (2025) Solar powered electric vehicle charging system: a comprehensive review. Discov Electron 2:96. https://doi.org/10.1007/s44291-025-00139-x

[9] Hossain MN, Cho HM (2026) Techno-economic feasibility of photovoltaic-powered electric vehicle charging stations: a global review and future outlook. Sustain Energy Res 13:9. https://doi.org/10.1186/s40807-025-00228-1

[10] Singla P, Boora S, Singhal P, et al (2024) Design and simulation of 4 kW solar power-based hybrid EV charging station. Sci Rep 14:7336. https://doi.org/10.1038/s41598-024-56833-5

[11] Singh S, Chauhan P, Singh NJ (2021) Feasibility of grid-connected solar-wind hybrid system with electric vehicle charging station. J Mod Power Syst Clean Energy 9(2):295–306. https://doi.org/10.35833/MPCE.2019.000081

[12] Singh B, Verma A, Chandra A, et al (2020) Implementation of solar PV-battery and diesel generator based electric vehicle charging station. IEEE Trans Ind Appl 56(4):4007–4016. https://doi.org/10.1109/TIA.2020.2989680

[13] Jain V, Singh B, Seema (2023) A grid connected PV array and battery energy storage interfaced EV charging station. IEEE Trans Transp Electrif 9(3):3723–3730. https://doi.org/10.1109/TTE.2023.3234994

[14] Shukl P, Singh B (2023) Distributed energy resources based EV charging station with seamless connection to grid. IEEE Trans Ind Appl 59(3):3826–3836. https://doi.org/10.1109/TIA.2023.3239583

[15] Sekhar KSR, Chaudhari MA, Khadkikar V (2023) Enhanced hybrid converter topology for PV-grid-EV integration. IEEE Trans Energy Convers 38(4):2634–2646. https://doi.org/10.1109/TEC.2023.3287890

[16] El-Taweel NA, Farag H, Shaaban MF, et al (2022) Optimization model for EV charging stations with PV farm transactive energy. IEEE Trans Ind Inform 18(7):4608–4621. https://doi.org/10.1109/TII.2021.3114276

[17] Bagherwal S, Mahapatra S (2024) Enhanced stability and control of solar powered EV charging stations using disturbance observer-based adaptive sliding mode control for DC voltage stabilization. IEEE Access 12:183293–183311. https://doi.org/10.1109/ACCESS.2024.3511637

[18] Swamynathan K, Mahalingam N, Paramasivam A, et al (2023) PV based off-grid charging station for E-vehicles using PWM and phase-shift controlled interleaved three-port converter. SN Appl Sci 5:331. https://doi.org/10.1007/s42452-023-05571-w

[19] Kancherla AB, Prasad NB, Kishore DR (2024) Solar energy EV charging system using integrated Zeta-Luo converter. J Eng Appl Sci 71:147. https://doi.org/10.1186/s44147-024-00477-9

[20] Mazumdar D, Shuaibu HA, Sain C, et al (2025) A novel and sturdy MPPT architecture for grid-tied EV charging stations using Ali Baba and forty thieves optimization. Discov Sustain 6:530. https://doi.org/10.1007/s43621-025-01089-w

[21] Karmakar A, et al (2025) Techno-economic analysis and optimized PV-powered EV charging facilities under various climate conditions in India. Discov Sustain 6:285. https://doi.org/10.1007/s43621-025-01119-7

[22] Ahamed M, et al (2026) Automated control integration of solar and wind energy for sustainable DC microgrid deployment in desert environments for EV charging. Discov Electron 3:46. https://doi.org/10.1007/s44291-026-00192-0

[23] Palanisamy S, Lala H (2024) Optimal sizing of renewable energy powered hydrogen and electric vehicle charging station (HEVCS). IEEE Access 12:48239–48254. https://doi.org/10.1109/ACCESS.2024.3383960

[24] Ullah Z, Yan L, Rehman AU, et al (2024) Distributed consensus-based optimal power sharing between grid and EV charging stations using derivative-free charging scheduling. IEEE Access 12. https://doi.org/10.1109/ACCESS.2024.3439019

[25] Ji D, Lv M, Yang J, et al (2020) Optimizing the locations and sizes of solar assisted electric vehicle charging stations in an urban area. IEEE Access 8:112772–112782. https://doi.org/10.1109/ACCESS.2020.3003071

[26] Reddy GH, Depuru SR, Gope S, et al (2023) Simultaneous placement of multiple rooftop solar PV integrated electric vehicle charging stations for reliability benefits. IEEE Access 11:130788–130801. https://doi.org/10.1109/ACCESS.2023.3335093

[27] Jiang Y, Ortmeyer T, Fan M (2023) Data-driven fast uncertainty assessment of distribution systems with correlated EV charging demand and renewable generation. IEEE Trans Sustain Energy 14(3):1446–1456. https://doi.org/10.1109/TSTE.2023.3236446

[28] Shalaby M (2025) Planning smart EV charging infrastructure around metro transit hubs in Riyadh. IEEE Access 13:201935–201947. https://doi.org/10.1109/ACCESS.2025.3638158

[29] Gunasekaran R, Manjunatha B, Anand S, et al (2024) Prediction of electric vehicle charging demand using enhanced gated recurrent units with RKOA based graph convolutional network. Discov Appl Sci 6:605. https://doi.org/10.1007/

s42452-024-06326-x

[30] Mahfouz MM, Iravani MR (2020) Grid-integration of battery-enabled DC fast charging station for electric vehicles. IEEE Trans Energy Convers 35(1):375–385. https://doi.org/10.1109/TEC.2019.2945293

[31] Mahfouz MM, Iravani R (2021) A supervisory control for resilient operation of the battery-enabled DC fast charging station and the grid. IEEE Trans Power Deliv 36(4):2532–2541. https://doi.org/10.1109/TPWRD.2020.3031859

[32] Arya H, Das M (2023) Fast charging station for electric vehicles based on DC microgrid. IEEE J Emerg Sel Top Ind Electron 4(4):1204–1212. https://doi.org/10.1109/JESTIE.2023.3285535

[33] Barsali S, Bojoi R, Ceraolo M, et al (2025) Grid forming inverters for electric vehicle charging stations to enhance distribution grid resilience. IEEE Access 13:109687–109700. https://doi.org/10.1109/ACCESS.2025.3582070

[34] Nisha KS, Gaonkar DN (2022) Model predictive controlled three-level bidirectional converter with voltage balancing capability for setting up EV fast charging stations in bipolar DC microgrid. Electr Eng 104:2653–2665. https://doi.org/10.1007/s00202-022-01492-w

[35] Sangeetha EP, Subashini N, Lindiya SA, et al (2026) A distinctive optimized sliding mode control approach for grid-connected bidirectional DC-DC converters in DC fast charging stations with G2V and V2G support. Electr Eng 108:262. https://doi.org/10.1007/s00202-026-03609-x

[36] Ashiq MMA, et al (2026) Artificial neural network controlled canonical switching converter for electric vehicle charging applications. Neural Comput Appl 38:306. https://doi.org/10.1007/s00521-026-12009-y

[37] Dakka O, Patthi S, Rao JVGR, et al (2024) A 5-kW unidirectional wireless power transfer EV charger with a novel multi-level PFC boost converter on front-end side. J Eng Appl Sci 71:7. https://doi.org/10.1186/s44147-023-00333-2

[38] Srivastava A, Manas M, Dubey RK (2023) Electric vehicle integration's impacts on power quality in distribution network and associated mitigation measures: a review. J Eng Appl Sci 70:32. https://doi.org/10.1186/s44147-023-00193-w

[39] Rajkumar S, Balasubramanian R, Kathirvelu KP (2025) A comparative analysis of supraharmonic emission by DC fast chargers used for electric vehicle charging. Sci Rep 15:7992. https://doi.org/10.1038/s41598-025-92049-x

[40] Tan AST, Ishak D, Mohd-Mokhtar R, et al (2018) Predictive control of plug-in electric vehicle chargers with photovoltaic integration. J Mod Power Syst Clean Energy 6:1264–1276. https://doi.org/10.1007/s40565-018-0411-7

[41] Verma A, Singh B (2021) AFF-SOGI-DRC control of renewable energy based grid interactive charging station for EV with power quality improvement. IEEE Trans Ind Appl 57(1):588–597. https://doi.org/10.1109/TIA.2020.3029547

[42] Srilakshmi K, Kondreddi K, Ramadevi A, et al (2025) Grid connected and standalone renewable source fed UPQC: a hybrid control technique for power quality enhancement. Discov Appl Sci 7:147. https://doi.org/10.1007/s42452-025-06562-9

[43] IEEE (2022) IEEE Std 519-2022: IEEE Standard for Harmonic Control in Electric Power Systems. IEEE, New York, https://doi.org/10.1109/IEEESTD.2022.9848440

[44] Shirguppikar S, Gavali P, Ganachari V, et al (2025) Characterization of Li-ion battery and state of charge estimation methods for diverse battery chemistries: a

review. Discov Appl Sci 7:1443. https://doi.org/10.1007/s42452-025-07906-1

[45] Louis GA, Sampathkumar S (2025) Predicting the state of charge of lithium ion battery in e-vehicles using Box-Jenkins combined artificial neural network model. Discov Appl Sci 7:129. https://doi.org/10.1007/s42452-024-06445-5

[46] Magdy M, Hanafy F, Abou-Zalam B, et al (2025) Optimized multi-stepped constant current constant voltage fast charging controller for lithium-ion batteries. Sci Rep 15:40359. https://doi.org/10.1038/s41598-025-25924-2

[47] Ye M, Gong H, Xiong R, et al (2018) Research on the battery charging strategy with charging and temperature rising control awareness. IEEE Access 6:64193–64201. https://doi.org/10.1109/ACCESS.2018.2876359

[48] Kennedy J, Eberhart R (1995) Particle swarm optimization. In: Proceedings of ICNN'95 International Conference on Neural Networks, vol 4. IEEE, Perth, pp 1942–1948, https://doi.org/10.1109/ICNN.1995.488968

[49] The MathWorks Inc. (2026) DC fast charger for electric vehicle. URL https://www.mathworks.com/help/simscape-electrical/ug/dc-fast-charger.html, simscape Electrical example, MATLAB R2026b. The MathWorks Inc., Natick

[50] The MathWorks Inc. (2026) Apply temperature-dependent cell parameter variations to battery module. Simscape Battery example, MATLAB R2026b. The MathWorks Inc., Natick

[51] The MathWorks Inc. (2026) Solar PV system with MPPT using boost converter. Simscape Electrical example, MATLAB R2026b. The MathWorks Inc., Natick

[52] IEC (2021) IEC 61724-1:2021 Photovoltaic System Performance – Part 1: Monitoring. International Electrotechnical Commission, Geneva

[53] ASHRAE (2014) ASHRAE Guideline 14-2014: Measurement of Energy, Demand, and Water Savings. ASHRAE, Atlanta

[54] Dobos AP (2014) PVWatts version 5 manual. Tech. Rep. NREL/TP-6A20-62641, National Renewable Energy Laboratory, Golden

[55] Plett GL (2004) Extended Kalman filtering for battery management systems of LiPB-based HEV battery packs: Part 3. State and parameter estimation. J Power Sources 134(2):277–292. https://doi.org/10.1016/j.jpowsour.2004.02.033

[56] Haykin S (2014) Adaptive Filter Theory, 5th edn. Pearson, Upper Saddle River

[57] Lu X, Chen M, Tian Y (2025) Accurate state-of-charge estimation of LiFePO4 battery: an adaptive extended Kalman filter approach using particle swarm optimization. Energy Rep 14:1169–1178. URL https://www.sciencedirect.com/science/article/pii/S2352484725004500

[58] Vendoti S, Tulasi NP, Jalli RK, et al (2025) Grid tied hybrid PV fuel cell system with energy storage and ANFIS based MPPT for smart EV charging. Sci Rep 15:27392. https://doi.org/10.1038/s41598-025-09626-3

[59] Duffie JA, Beckman WA (2013) Solar Engineering of Thermal Processes, 4th edn. Wiley, Hoboken

[60] Teodorescu R, Blaabjerg F, Liserre M, et al (2006) Proportional-resonant controllers and filters for grid-connected voltage-source converters. IEE Proc Electr Power Appl 153(5):750–762

[61] Ciobotaru M, Teodorescu R, Blaabjerg F (2006) A new single-phase PLL structure based on second order generalized integrator. In: Proceedings of the 37th IEEE Power Electronics Specialists Conference (PESC). IEEE, Jeju, pp 1–6

[62] CENELEC (2010) EN 50530:2010 Overall Efficiency of Grid Connected Photovoltaic Inverters. CENELEC, Brussels

[63] Hampel FR (1974) The influence curve and its role in robust estimation. J Am Stat Assoc 69(346):383–393

[64] Meinel AB, Meinel MP (1976) Applied Solar Energy: An Introduction. Addison-Wesley, Reading

[65] Mahindra Last Mile Mobility Ltd. (2025) Mahindra Treo electric three-wheeler: technical specifications (48 V, 7.37 kWh lithium-ion battery). URL https://www.mahindralastmilemobility.com/, mahindra, Mumbai

[66] Central Electricity Authority (2024) CO_2 baseline database for the Indian power sector, user guide, version 20.0. URL https://cea.nic.in/wp-content/uploads/2021/03/User_Guide_Version_20.0.pdf, ministry of Power, Government of India, New Delhi

[67] India Meteorological Department (2026) Statement on the climate of India during 2025. URL https://wmo.int/media/news-from-members/statement-climate-of-india-during-2025, world Meteorological Organization, News from Members, 12 January 2026

[68] Xu P, Wang X, Li Z (2025) Impact and optimization of vehicle charging scheduling on regional clean energy power supply network management. Energy Inform 8:13. https://doi.org/10.1186/s42162-025-00476-x

[69] Hao F (2025) Impact of electric vehicle charging demand on clean energy regional power grid control. Energy Inform 8:83. https://doi.org/10.1186/s42162-025-00538-0

[70] Zheng D, Zheng B (2025) Optimization of electric vehicle charging facility layout considering the enhancement of renewable energy consumption capacity and improvement of PSO algorithm. Energy Inform 8(1). https://doi.org/10.1186/s42162-025-00514-8

[71] Ostermann A, Haug T (2024) Probabilistic forecast of electric vehicle charging demand: analysis of different aggregation levels and energy procurement. Energy Inform 7(1):1–25. https://doi.org/10.1186/s42162-024-00319-1

[72] Künsch HR (1989) The jackknife and the bootstrap for general stationary observations. Ann Stat 17(3):1217–1241. https://doi.org/10.1214/aos/1176347265